

Secondary organic aerosol formation from smoldering and flaming combustion of biomass: a box model parametrization based on volatility basis set

Giulia Stefenelli¹, Jianhui Jiang¹, Amelie Bertrand^{1,2,3}, Emily A. Bruns^{1,a}, Simone M. Pieber^{1,4}, Urs Baltensperger¹, Nicolas Marchand², Sebnem Aksoyoglu¹, André S. H. Prévôt¹, Jay G. Slowik¹, and Imad El Haddad¹

¹ Laboratory of Atmospheric Chemistry, Paul Scherrer Institute (PSI), 5232 Villigen, Switzerland

² Aix Marseille Univ, CNRS, LCE, Marseille, France

¹⁰ ³Agence de l'Environnement et de la Maîtrise de l'Energie 20, avenue du Gresillé – BP 90406, 49004 Angers Cedex 01, France

⁴ Empa, Laboratory for Air Pollution and Environmental Technology, 8600 Dübendorf, Switzerland

^a now at: Washington State Department of Ecology, Lacey, WA, USA

Correspondence to: Imad El Haddad (imad.el-haddad@psi.ch), Jay G. Slowik (jay.slowik@psi.ch) and Jianhui Jiang (jianhui.jiang@psi.ch)

15

20

Abstract

Residential wood combustion remains one of the most important sources of primary organic aerosols (POA) and secondary organic aerosol (SOA) precursors during winter. The overwhelming majority of these precursors have not been traditionally considered in regional models, and only recently, lignin pyrolysis products and polycyclic aromatics were identified as the 5 principal SOA precursors from flaming wood combustion. The SOA yields of these components in the complex matrix of biomass smoke remain unknown and may not be inferred from smog chamber data based on single compound systems. Here, we studied the aging of emissions from flaming and smoldering-dominated wood fires in three different residential stoves, across a wide range of aging temperatures (-10°C, 2°C and 15°C) and emission loads. Organic gases (OGs) acting as SOA precursors were monitored by a proton transfer reaction time-of-flight mass spectrometer (PTR-TOF-MS), while the evolution 10 of the aerosol properties during aging in the smog chamber was monitored by a high resolution time-of-flight aerosol mass spectrometer (HR-ToF-AMS). We developed a novel box model based on the volatility basis set (VBS) to determine the volatility distributions of the oxidation products from different precursor classes found in the emissions, grouped according to their emission pathways and SOA production rates. We show for the first time that SOA yields in complex emissions are consistent with those reported in literature from single compound systems. We identify the main SOA precursors in both 15 flaming and smoldering wood combustion emissions at different temperatures. While single-ring and polycyclic aromatics are significant precursors in flaming emissions, furans generated from cellulose pyrolysis appear to be important for SOA production in the case of smoldering fires. This is especially the case at high loads and low temperatures, given the higher volatility of furan oxidation products predicted by the model. We show that the oxidation products of oxygenated aromatics from lignin pyrolysis are expected to dominate SOA formation, independent of the combustion or aging conditions, and 20 therefore can be used as promising markers to trace aging of biomass smoke in the field. The model framework developed herein may be generalizable for other complex emissions sources, allowing determination of the contributions of different precursor classes to SOA, at a level of complexity suitable for implementation in regional air quality models.

1. Introduction

Atmospheric aerosols impact visibility, human health, and climate on a global scale (Stocker et al., 2013; World Health 25 Organization, 2013). A thorough understanding of their chemical composition, sources, and processes is a fundamental prerequisite to develop appropriate mitigation policies. Laboratory experiments using smog chambers enable the detailed examination of the gas-phase composition and aging of different emissions such as biomass smoke (e.g. Bruns et al., 2016; Bian et al., 2017), car exhaust (Gordon et al., 2014a ; b, Platt et al., 2017 ; Gentner et al., 2017; Pieber et al., 2018), aircraft exhaust (Miracolo et al., 2011; Kılıç et al., 2018), or cooking emissions (Klein et al., 2016). Results from these studies 30 consistently show that the measured concentrations of secondary organic aerosol (SOA), formed upon oxidation and partitioning of the oxidized vapors, greatly exceed estimated concentrations based on the oxidation of volatile organic compounds (VOCs) traditionally assumed to be the dominant SOA precursors (Jathar et al., 2012). The SOA formed from

these chemically speciated VOCs is defined as traditional SOA (T-SOA) and is explicitly accounted for in chemical transport models (CTMs). However, Robinson et al. (2007) suggested that a significant fraction of the unexplained SOA is due to the oxidation of lower-volatility organics, i.e. semi-volatile and intermediate volatility organic compounds (SVOC and IVOC, respectively), collectively referred to as non-traditional SOA (NT-SOA) precursors (Donahue et al., 2009).

5 In spite of its importance, incorporating NT-SOA into current organic aerosol (OA) models remains challenging without the identification and the quantification of the most important precursors (Jathar et al., 2012). For simplification purposes several methods based on the volatility of the emissions and a volatility-based oxidation mechanism have been developed. Currently the volatility basis set (VBS) scheme is considered to be the most suitable approach to simulate the aging processes of non-speciated organic vapors (Donahue et al., 2006). The VBS scheme represents OA as a discrete volatility-resolved mass 10 distribution. Reactions are described by the transfer of OA mass between volatility bins, thereby accounting for the contribution of non-traditional vapors to SOA formation without the need to incorporate explicit chemical mechanisms. Robinson et al. (2007) proposed that SVOCs, IVOCs and their products react with hydroxyl radicals (OH) to form products that are an order of magnitude lower in volatility than their precursors. Pye and Seinfeld (2010) proposed a single-step mechanism for the non-speciated SVOCs, where the products of oxidation were two orders of magnitude lower in volatility than the precursors. They 15 used SOA-yield (defined as SOA mass formed divided by reacted precursor mass) data for naphthalene as a surrogate for all non-speciated IVOCs, even though these are thought to be mainly branched and cyclic alkanes (Robinson et al., 2007, 2010; Schauer et al., 1999). Both methods have been implemented in plume models as well as regional and global chemical transport models and have reduced discrepancies between measured and predicted SOA concentrations and properties (Shrivastava et al., 2008; Dzepina et al., 2009; Pye and Seinfeld, 2010; Jathar et al., 2011). However, considerable uncertainties remain in the 20 relative contributions of non-traditional precursors to different emissions, their ability to form SOA and their reaction rate constants (Jathar et al., 2014a). Limitations in SOA modelling are also a direct consequence of limitations in measurements; namely undetected or unidentified precursors and limited number of studies available investigating the influence of different parameters such as temperature, emission load, and combustion regimes. For instance, the overwhelming majority of smog chamber studies have been conducted under summer-time conditions (20-30°C), preventing the assessment of temperature 25 effects on both SOA-producing reactions and the partitioning thermodynamics (Jathar et al., 2013).

Similar limitations apply to the consideration of emissions in models. Biomass combustion is a major source of gas and particle-phase air pollution on urban, regional and global scales (Grieshop et al., 2009; Lanz et al., 2010; Crippa et al., 2013; Gobiet et al., 2014; Chen et al., 2017; Bozzetti et al., 2017). Globally, approximately 3 billion people burn biomass or coal for residential heating and cooking (World Energy Council, 2016), often using old and highly polluting appliances. Emissions 30 from these devices are highly variable depending on fuel type and fuel moisture (McDonald et al., 2000; Schauer et al., 2001; Fine et al., 2002; Pettersson et al., 2011; Eriksson et al., 2014; Reda et al., 2015; Bertrand et al., 2017), and typically include a complex mixture of non-methane organic gases (NMOGs), primary organic aerosol (POA), and black carbon (BC). Once emitted into the atmosphere, organic compounds can react with oxidants such as OH radicals, ozone (O_3) and nitrate radicals (NO_3). These reactions remain poorly understood, which greatly hinders the quantification of wood combustion SOA in

ambient air. Bruns et al. (2016) investigated the SOA formation from residential log wood combustion from a single type of stove under stable flaming conditions only. They reported that T-SOA precursors included in models account for only 3 to 27% of the measured SOA whereas 84 to 116% was from NT-SOA precursors including in total 22 individual compounds and two lumped compound classes, mainly consisting of polycyclic aromatic hydrocarbons from incomplete combustion (e.g. 5 naphthalene) and cellulose and lignin pyrolysis products (e.g. furans and phenols, respectively). The estimated SOA concentrations were based on the literature SOA yields of single precursors, obtained from smog chamber experiments, and a good agreement was observed between predicted and measured SOA. However, the method suffers from two drawbacks. First, the dependence of the yields on the organic aerosol loading and temperature was not considered. Second, although the relative 10 contributions of different precursors to SOA were estimated, thermodynamic parameters for chemical transport models (CTMs) were not determined. Based on the same experiments, the lumped concentrations of the 22 non-traditional volatile organic compounds and 2 compound classes were constrained in a box model (Ciarelli et al., 2017a). Improved parameters were retrieved describing the volatility distributions and the production rates of oxidation products from the overall mixture 15 of precursors present in biomass smoke. While this method is well suited for CTMs (Pandis et al., 2013; Ciarelli et al., 2017b), it does not provide any information about the contributions of the different chemical classes to the aerosol. Similar limitations 20 are associated with the study of other emissions, e.g. fossil fuel combustion or evaporation (Jathar et al., 2013, 2014b). The development of models capable of simulating the contribution of the different chemical species to the aerosol at different conditions is especially important in the light of the current development of highly time resolved chemical ionization mass spectrometry, capable of quantifying these products. To realize the full potential of the data acquired by this instrumentation, a modelling framework capable of predicting the production rates and the partitioning between the gas and the particle phase 25 of the oxidation products from complex emissions is required.

Here, we extend the past analysis investigating the most recent smog chamber data of residential wood combustion based on 14 experiments performed in 2014-2015 under various conditions. Different experimental temperatures of the smog chamber were investigated; namely -10°C, 2°C and 15°C. Three different stove types were tested, including conventional and modern 20 residential burners. Different emission load and different hydroxyl (OH) radical exposure were examined. Moreover distinct combustion regimes were sampled across the different experiments for the first time, to investigate the secondary organic 25 aerosol chemical composition and yields from flaming and smoldering emissions. Integrated VBS-based model and novel parameterization methods based on a genetic algorithm (GA) approach were developed to predict the contribution of the oxidation products of different chemical classes present in complex emissions and to better explain the SOA formation process, providing useful information to regional air quality models. Overall, this study presents a general framework which can be 30 adapted to assess SOA closure for complex emissions from different sources.

2 Methods

2.1 Smog chamber set up and procedure

Two smog chamber campaigns were conducted to investigate SOA production from multiple domestic wood combustion appliances as a function of combustion phase, initial fuel load, and OH exposure. These experiments were previously described in detail (Bruns et al., 2016; Ciarelli et al., 2017; Bertrand et al., 2017, 2018a) and are summarized here. Experiments from Bertrand et al. (2017, 2018a) will be referred to as Set1 and experiments from Bruns et al. (2016) and Ciarelli et al. (2017) as Set2.

The emissions were generated by three different logwood stoves for residential wood combustion: stove 1 manufactured before 2002 (Cheminées Gaudin Ecochauff 625), stove 2 fabricated in 2010 (Invicta Remilly) and stove 3 (Avant, 2009, Attika). For each stove three to four replicate experiments were performed with a loading of 2-3 kg of beech wood having a total moisture content ranging between 2 and 19%. The fire was ignited with 3 starters made of wood wax, wood shavings, paraffin and natural resin. The starting phase was not studied. In total, 14 experiments were performed, consisting of two experiments at -10°C, seven experiments at 2°C and five experiments at 15°C. These experiments cover the typical range of European winter temperatures and are summarized in Table 1.

Ward and Hardy (1991) define the flaming and smoldering conditions according to the modified combustion efficiency, MCE = $\text{CO}_2/(\text{CO}+\text{CO}_2)$. Specifically, MCE > 0.9 is identified as flaming condition, while MCE < 0.85 is identified as smoldering condition. MCE values for the different experiments are reported in Table 1. According to this parameter, Set1 and Set2 experiments were dominated by smoldering and flaming, respectively. Practically, we achieved the different burning conditions by varying the amount of air in the stoves, therefore changing the combustion temperature. For Set1, closing the air window decreased the flame temperature, resulting in a transition from a flaming to a smoldering fire. This could be visibly identified, together with the development of a thick white smoke from the chimney. We note that this conduct is very common in residential stoves, to keep the fire running for longer. Meanwhile, for Set2, after lighting the fire, we kept a high air input to maintain a flaming fire. At the same time, we monitored the MCE in real time and only injected the emissions into the chamber when the MCE increased above 0.9.

The experiments were performed in a flexible Teflon bag of nominally 7 but typically about 5.5 m³ equipped with UV lamps (40 lights, 90–100W, Cleo Performance, Philips, wavelength $\lambda < 400$ nm) enabling photo-oxidation of the emissions (Platt et al., 2013; Bruns et al., 2015). The chamber is located inside a temperature-controlled housing. Relative humidity was maintained at 50% and three different temperatures were investigated. Emissions from the stoves were sampled from the chimney into the chamber through heated (140°C) stainless-steel lines to reduce the loss of semi-volatile compounds. An ejector dilutor was installed (Dekati Ltd, DI-1000) to dilute emissions in the chamber by a factor of 10 before sampling. The sample injection lasted for approximately 30 minutes for each experiment, and were followed by an injection of 1 µL d9-butanol (98%, Cambridge Isotope Laboratories), which was used to estimate the OH exposure as described in Section 3.1.1 (Barmet et al., 2012). The chamber was then allowed to equilibrate for 30 minutes to ensure stabilization and homogeneity

and to fully characterize the primary emissions before aging. OH radicals were produced by UV irradiation of nitrous acid (HONO) injected after chamber equilibration, generated as described in Taira and Kanda (1990), reaction of diluted sulfuric acid (H_2SO_4) and sodium nitrate (NaNO_2) in a gas flask, and introduced into the chamber and brought into the gas-phase flushing with a carrier gas with a flow rate of 1 L min⁻¹. The smog chamber was then irradiated with UV lights for 5 approximately 4 hours to simulate atmospheric aging.

Before and after each experiment, the smog chamber was cleaned with humidified pure air (100% RH) and O_3 (1000 ppm) under irradiation with UV lights for at least 1 hour, followed by flushing with pure dry air for at least 10 hours. The background particle- and gas-phase concentrations were then measured in the clean chamber.

The total amount and composition of the emissions depend on the oxygen supply, temperature, the fuel elemental composition, 10 and combustion conditions, which can be broadly classified as flaming or smoldering (Koppmann et al., 2005; Sekimoto et al., 2018). Flaming combustion occurs at high temperature and consists of volatilization of hydrocarbons from the thermal decomposition of biomass leading to rapid oxidation and efficient combustion, producing CO_2 , water and black carbon (BC). Instead, smoldering combustion is flameless and can be initiated by weak sources of heat and results in less efficient combustion of fuel, leading to gas-phase products (mainly CO, CH_4 and volatile organic compounds).

15 2.2 Instrumentation

We characterized the emissions with a suite of gas- and particle-phase instrumentation. Organic gases (OGs) were measured by a proton transfer reaction time-of-flight mass spectrometer (PTR-ToF-MS 8000, Ionicon Analytik). A detailed description of the instrument can be found in Jordan et al. (2009). The PTR-ToF-MS was operated under standard conditions (ion drift pressure of 2.2 mbar and drift intensity of 125 Td) in H_3O^+ mode, allowing the detection of OGs with a proton affinity higher 20 than that of water. For quantification, when known individual reaction rate constants were used (Cappellin et al., 2012), otherwise a value of $2 \times 10^{-9} \text{ cm}^3 \text{ s}^{-1}$ was assumed. The effectively rate constants applied to both Set1 and Set2 can be found in Bruns et al., (2017). Data were analyzed using the Tofware software 2.4.2 (PTR module as distributed by Ionicon Analytik GmbH, Innsbruck, Austria) running in Igor Pro 6.3.

Non-refractory primary and aged particle composition was monitored by a high resolution time-of-flight aerosol mass 25 spectrometer (HR-ToF-AMS, Aerodyne Research Inc.) (DeCarlo et al., 2006). The HR-ToF-AMS is described in detail elsewhere (Bruns et al., 2016; Bertrand et al., 2017) and summarized here. The instrument was operated under standard conditions (temperature of vaporizer 600°C, electronic ionization (EI) at 70eV, V mode) with a temporal resolution of 10 seconds. Data analysis was performed in Igor Pro 6.3 (Wave Metrics) using SQUIRREL 1.57 and PIKA 1.15Z assuming a collection efficiency of 1. The O:C ratio was determined according to Aiken et al. (2008).

30 Black carbon (BC) was derived from the absorption coefficient measured with a 7-wavelength aethalometer (Magee Scientific aethalometer model AE33). The corresponding mass concentration of equivalent BC (eBC) was thus converted from the absorption coefficient measured with a time resolution of 1 minute at a wavelength of 880 nm (Drinovec et al., 2015).

The particle number concentration and size distribution (16 to 914 nm) were provided by a scanning mobility particle sizer (SMPS, consisting of a custom-built differential mobility analyzer (DMA) and a condensation particle counter (CPC 3022, TSI)) with a time resolution of 5 minutes. Supporting gas measurements included a CO₂ analyzer (LI-COR), a CH₄, a total hydrocarbon (THC) monitor (flame ionization detector, THC monitor Horiba APHA-370), and NO and NO₂ (NO_x analyzer, 5 Thermo Environmental) monitors.

3. Data analysis

The data analysis entails three steps detailed in this Section: The first sub-section describes the determination of the amount of oxidized OGs in the chamber. The second sub-section details the determination of the amount of SOA formed in the chamber. The last sub-section describes the box model used for the parameterization of SOA formation from the OGs.

10 3.1 Organic gases loss in the chamber

In the chamber, OGs were oxidized to several oxidation products, referred to as oxidized OGs (CG, condensable gases) in the following analysis. According to their volatility, these products may remain in the gas phase or partition to the particle phase, thereby contributing to SOA formation.

We described the change in any OG concentration over time as a combination of its loss and production as follows:

$$15 \frac{d[OG]}{dt} = P - \left(\sum k_{dil} * [OG] + k_{OH} * [OH] * [OG] + k_{other} * [OG] \right) \quad (1)$$

Here, P corresponds to the production of a OG in the chamber, e.g. from the oxidation of other primary OGs. k_{dil} is the dilution rate constant in s⁻¹. $k_{OH}[OH] [OG]$ in molec⁻¹ cm³ s⁻¹ represents the consumption rate due to oxidation by OH, where k_{OH} is the reaction rate constant and [OH] is the OH concentration. $k_{other}[OG]$ in molec⁻¹ cm³ s⁻¹ is the loss rate of OG by other processes, where k_{other} is the reaction rate constant in s⁻¹. The loss of some OGs could not be explained by their reaction with OH and dilution alone for the Set1, so we added this additional term which is discussed after the first two processes are constrained. We considered primary OGs that exhibited a clear decay with time to be strictly of primary origin, and hence neglected their production from other OGs (i.e. $P = 0$). This assumption signifies that the yields estimated under our conditions are upper limits. In reality, the detection of aromatic hydrocarbons (e.g. single-ring aromatic hydrocarbons, SAHs and 20 polycyclic aromatic hydrocarbons, PAH) by the PTR-ToF-MS may be affected by the interference due to fragmentation during ionization of their oxidation products (Gueneron et al., 2015). On the other hand, directly emitted oxygenated aromatics could be themselves the oxidation products of aromatic hydrocarbons and their production may continue during the experiment. 25 However, the assumption of $P = 0$ does not introduce a significant error for most OGs with significant primary emissions, because the observed OG decay was consistent with their OH reaction rate constant for Set 2 as demonstrated by Bruns et al.

(2017) for the +15°C conditions. In the following, we describe the processes governing the changes in the OG concentrations in the chamber and the approaches adopted for the determination of the different parameters in Eq. (1).

3.1.1 Reaction with OH radical

The OH exposure, that is the integrated OH concentration over time, was estimated based on the differential reactivity of two OGs. Specifically, we used d9-butanol (fragment at mass to charge ratio m/z 66.126, $[C_4D_9]^+$) and naphthalene (fragment at m/z 129.070, $[C_{10}H_8]H^+$). These compounds are selected because they can be unambiguously detected (no isomers or interferences, high signal-to-noise), are not produced during the experiment, and have OH reaction rate constants that are precisely measured and significantly different from each other. The OH exposure can be expressed as follows:

$$OH \text{ exposure} = \left(\frac{\ln \left(\frac{d9 - \text{butanol}}{\text{naphthalene}} \right)_0 - \ln \left(\frac{d9 - \text{butanol}}{\text{naphthalene}} \right)_t}{k_{OH, \text{but}} - k_{OH, \text{naph}}} \right) \quad (2)$$

where $(d9\text{-butanol}/\text{naphthalene})_0$ is the ratio between these compounds at $t = 0$ (before lights were turned on), $(d9\text{-butanol}/\text{naphthalene})_t$ is the ratio measured at time t , and $k_{OH, \text{but}}$ and $k_{OH, \text{naph}}$ are the OH reaction constants of d9-butanol and naphthalene, respectively ($k_{OH, \text{but}} = 3.14 \times 10^{-12} \text{ cm}^3 \text{ molec}^{-1} \text{ s}^{-1}$ and $k_{OH, \text{naph}} = 2.30 \times 10^{-11} \text{ cm}^3 \text{ molec}^{-1} \text{ s}^{-1}$) (Atkinson and Arey, 2003).

For Set1, the OH exposure at the end of each experiment ranged between 5 and $8 \times 10^6 \text{ molec cm}^{-3} \text{ h}$, corresponding to approximately 5-8 hours in the atmosphere (given global average and typical wintertime OH concentrations of $1 \times 10^6 \text{ molec cm}^{-3}$). For Set2, higher OH exposures were reached (3 to $7 \times 10^7 \text{ molec cm}^{-3} \text{ h}$ at the end of each experiment, corresponding to 2-3 days in the atmosphere). This is likely because both sets of experiments utilized a similar HONO molar flow (and thus similar OH production rate), but higher OG concentrations were reached in Set1, which could possibly have resulted in a higher OH sink. We calculated the OH concentration, $[\text{OH}]$ in Eq. (1), numerically as $d(\text{OH exposure})/dt$.

3.1.2 Smog chamber dilution

For Set 2, dilution was dominated by the constant injection of HONO to the chamber and accounted for as described in Bruns et al. (2016). For Set1 the dilution rate of primary OGs in the chamber was calculated as follows. The integrated dilution over time, K_{dil} , was determined as the ratio between the d9-butanol concentration corrected for the reaction of d9-butanol with OH and the d9-butanol concentration at $t = 0$ ($[d9\text{-butanol}]_0$):

$$K_{dil} = \frac{[d9 - \text{butanol}] * e^{k_{OH, \text{but}} * OH \text{ exposure}}}{[d9 - \text{butanol}]_0} \quad (3)$$

Figure S1 shows calculated values for K_{dil} as a function of time. Increasingly high dilution at the end of these experiments (Fig S1), between 20 and 35% (i.e., a dilution ratio of 0.8 to 0.65), is a result of constant injection of HONO and excessive sampling at high rates, resulting in inputs from laboratory air (likely through leaks in the Teflon bag or the connections of chamber inlets and outlets). The inputs from the HONO pure carrier gas and of laboratory air are roughly comparable (about 12 vs. 8-23% at 5 the end of the experiment). Besides dilution, the effect of both inputs on the gas phase chemical composition is negligible. Dilution rates are non-linear, increasing as the experiment progresses due to continuous dilution within a decreasing chamber volume. The dilution rate constant, k_{dil} , in Eq. (1), is the differential of K_{dil} over time.

3.1.3 Losses by other processes

To corroborate the estimated OH exposures and dilution rates, we examined the loss of prominent OGs with known reaction 10 rate constants against OH. For Set2 and as demonstrated by Bruns et al. (2017), the OG decay is consistent with their estimated loss based on their dilution and reaction with OH. By contrast, for Set1, the decay of some OGs could not be solely explained by their reaction with OH and dilution, suggesting additional reactions with oxidants other than OH as discussed below. The OG total consumption by this process ($\int k_{other} [OG]$) was estimated as the difference between the total measured decay of 15 the OG of interest and the fraction consumed by both dilution and oxidation by OH radicals. The reaction rate constants for several precursors towards OH (k_{OH}) are not available in the literature. In addition, many fragments may have several isomers, each of which associated with different rate constants. Effective rate constants for all precursors considered were estimated from their decay in Set2, where the combination of OH reaction and dilution fully explained the decay of OGs with known OH reaction rate constants.

3.1.4. Precursor classification

20 A common set of 263 ions were extracted from the PTR-ToF-MS. Among these ions, 86 showed a clear decay with time and were thus identified and selected as potential SOA precursors. Previous work based on Set2 experiments showed that the PTR-ToF-MS measures the most important SOA precursors, which explained the measured SOA mass within 40% uncertainty and without systematic bias (Bruns et al., 2016). Therefore, these compounds are expected to capture the dominant fraction of SOA 25 mass, although we cannot rule out losses in the PTR-ToF-MS inlet or small contributions from other precursors such as alkanes. The compound identification was supported by previous publications (McDonald et al., 2000; Fine et al., 2001; Nolte et al., 2001; Schauer et al., 2001; Stockwell et al., 2015), including gas chromatography-mass spectrometry (GC-MS) analysis when 30 available.

The size of our dataset does not allow us retrieving the volatility distribution for single precursors, which would entail the determination of more than 86 free parameters. This is especially the case as the time series of precursors, decaying with oxidation, are typically strongly correlated, which prevents resolving systematic differences between the yields of the different single precursors. Therefore, lumping is needed to decrease the model degree of freedom. Accordingly, precursors are grouped

in six chemical classes: furans, single-ring aromatic hydrocarbons (SAH), polycyclic aromatic hydrocarbons (PAH), oxygenated aromatics (OxyAH) and organic compounds containing more or less than 6 carbon atoms (OVOC_{c≥6}, OVOC_{c<6}, respectively) (Table S1). The selected precursors in each class are the same for each experiment and each dataset. This lumping approach is based on the two main objectives of the study:

5 1. Compare the SOA yields of specific precursors determined in complex emission experiments with those determined in single compound systems.

2. Identify the main SOA precursors in flaming and smoldering wood emissions, at different temperatures.

To be able to compare to literature yields, we lumped species that have similar yields in the same chemical class: e.g. at organic aerosol concentration of 10 $\mu\text{g m}^{-3}$ the yields of PAHs is ~20% (objective 1). In addition, we classified the precursors based

10 on the pathway by which they are emitted, which will allow us to determine which compounds dominate SOA formation in flaming and smoldering emissions (objective 2). We differentiated between oxygenated aromatics, mainly emitted through lignin pyrolysis, furans emitted through cellulose pyrolysis and single-ring aromatics and PAHs generated from incomplete combustion, especially from flaming wood. The remaining SOA precursors are all oxygenated OGs therefore we separated them according to their carbon number knowing that larger precursors will have higher yields than smaller precursors. Our

15 ability to precisely extract yields specific to a precursor class heavily relies on differences in the oxidation rates or emission patterns of the precursors. Therefore, the classification approach adopted here, where classes are expected to have different contributions during different experiments (Bhattu et al., 2019), facilitates the extraction of yields of the different classes.

3.2 Calculation of the OA mass in the chamber

The total organic aerosol measured by the HR-ToF-AMS was corrected for particle losses in the chamber due to gravitational and diffusional deposition. To assess the total wall losses due to both processes, we assumed that the condensable vapors partition only to the suspended aerosols but not to the wall.

Assuming that black carbon is inert in the chamber, it was possible to use its decay to estimate the particle loss to the walls. The aerosol attenuation measured at 880 nm (at the end of each experiment, ~4 hours) with an aethalometer was used to estimate the particle loss rate to the wall. This attenuation is proportional to the eBC mass concentration and within 25 uncertainties independent of the aging extent, as demonstrated in Kumar et al. (2018). Using eBC as a tracer, we inherently assumed that eBC and OA were internally mixed and homogeneously distributed over the aerosol size range. The decay of eBC due to both dilution and deposition onto the chamber walls was parametrized as follows:

$$\frac{d[\text{eBC}]}{dt} = -k_{\text{dil}} [\text{eBC}] - k_{\text{wall}} [\text{eBC}] \quad (4)$$

where k_{wall} is the first order wall loss rate used to correct the measured OA concentration for wall losses, ranging between 4 and $8 \times 10^{-5} \text{ s}^{-1}$, and k_{dil} is the dilution rate determined above.

The wall loss corrected organic aerosol, OA_{WLC}, was calculated using Eq. (5):

$$OA_{WLC}(t) = OA(t) + \int_0^t k_{wall} * OA(t) * dt \quad (5)$$

where OA(*t*) is the measured organic aerosol concentration in $\mu\text{g m}^{-3}$. The total OA present in the chamber was estimated as the suspended OA concentration measured by the HR-ToF-AMS plus the estimated OA lost to the wall. This concentration was directly compared to the condensable gases (CG) concentration estimated according to Eq. (A8) presented in the Appendix A. As mentioned, our approach did not take into account the losses of precursor vapors or their oxidation products in the gas phase onto the walls. We note that these processes were unlikely to have a substantial effect on the precursors considered, which were largely highly volatile species, even at lower temperature. Based on the calculation of the equilibrium constant of semi-volatile species on the walls by Bertrand et al. (2018b), we estimated that at 293 K the fraction of these compounds absorbed on the walls is <5%. Meanwhile, the walls could indeed act as a sink for the semi-volatile oxidation products. This effect was not taken into account in the current study, but we expect that it was minimized under our conditions, by the high OA concentration in the chamber and rapid production rates (Zhang et al., 2014; Nah et al., 2017).

3.3. Modelling SOA formation

The general aim of the model is the determination of the parameters describing the volatility distributions of the oxidation products from different precursor classes and their temperature-dependence. A simplified schematic of the modeling framework is described in Fig. 1. It consists of 1) a box model that describes the partitioning of the condensable gases generated through oxidation, 2) the model input parameters obtained from the smog chamber, 3) the model output parameters and 4) the model optimization based on a genetic algorithm (GA). Each of these parts is described in the following sections.

3.3.1 Box model

We assume the partitioning of CG between the gas and the particle phases to obey Raoult's law (Strader et al., 1999), where the aerosol can be described as a pseudo-ideal organic solution, of SOA and POA species. The volatility basis set (VBS, implemented by Koo et al., 2014 in the Comprehensive Air quality Model with eXtensions, CAMx), was used to classify the oxidation products of the different precursors into surrogates with different volatility, distributed into discrete logarithmically spaced bins (Donahue et al., 2006).

We considered the most basic mechanism by which SOA may form. That is, the oxidation products from the different precursor classes described above instantaneously partition into the condensed phase depending on their volatility. No additional reactions in the gas or particle phase were considered (e.g. reaction with oxidants, photolysis or oligomerization). In addition, we neglected the contribution of primary oxidation products of the gas-phase semi-volatile species (co-emitted with POA) compared to the OGs detected by the PTR-ToF-MS, based on the findings of Bruns et al. (2016) and Ciarelli et al. (2017).

Finally, we considered the species in the gas and the particle phase to be permanently at equilibrium, as condensation is expected to be faster than oxidation (time scales for oxidized vapours condensation < 1 minute assuming no particle phase diffusion limitations, Bertrand et al., 2018b). While including additional processes in the model is feasible, this would result in a significantly higher-dimensional parameter space, which cannot be unambiguously inferred from the present data. We 5 consider that without supportive data, e.g. chemically resolved characterization of the particle phase species, such reactions could not be well constrained or even deduced from structure activity relationships, given the many unknowns in complex emissions. Therefore, such simplified scheme of SOA formation from complex emissions may be compared in the future with chemically resolved data to help the identification of additional mechanisms that were not considered here.

The derivation of the thermodynamic equations governing SOA formation from precursors, implemented in the box model, is 10 detailed in Appendix A and only a brief description of the model principles is given here. In the following, let i and j be the indices for the different volatility bins and precursor classes, respectively. The model determines the molar distribution of the oxidation products from different precursor classes in the different volatility bins, $Y_{i,j}$, together with the compounds' enthalpy of evaporation, $\Delta H_{vap\ i,j}$. The latter describes the temperature dependence of the oxidation products' effective molar saturation concentration, $x_{i,j}^*$. For this, the model iteratively solves Eq. (A6) and (A7) at every experimental time step (time resolution of 15 10 seconds) for all experiments, to retrieve the surrogate molar concentrations in the particle phase, $x_{i,j}|_p$ and the total surrogates' molar concentration in the condensed organic phase, x_{OA} (see Appendix A).

3.3.2 Model inputs

The model uses as main inputs the molar concentrations of the condensable gases from different precursors (in total $n = 6$ precursor classes) in both phases, $x_j|_{g+p}$. The latter is derived from the consumption rates of VOC_j determined by the PTR- 20 ToF-MS, by numerically integrating Eq. A8. $x_j|_{g+p}$ is related to the concentrations of the different surrogates from a precursor class j in different volatility bins, $x_{i,j}|_{g+p}$ (Eq. A6), through their yields, $Y_{i,j}$, according to Eq. A9. The number of volatility bins, m , is set to 6, approximately corresponding to the following mass saturation concentrations: $\overrightarrow{C_{i,j}^*}(\mu\text{g m}^{-3}) = \{10^{-1}; 10^0; 10^1; 10^2; 10^3; 10^4\}$.

In addition to $x_j|_{g+p}$, the model needs as inputs $x_i^{OM_p}|_{p+g}$, the molar concentration of primary organic matter from a volatility 25 bin i in both gas and particle phase (Eq. A7). $x_i^{OM_p}|_{g+p}$ is inferred from the measured POA concentrations injected in the chamber at the beginning of the experiment and using the volatility distribution function of wood combustion emissions in May et al. (2013). It is assumed constant with aging. The computation of the fraction of POA_i in the condensed phase is similar to that for SOA species in Eq. (A6).

The secondary surrogates' elemental composition ($C\#_{i,j}$, $O\#_{i,j}$ and $H\#_{i,j}$) is also used as model inputs to compute the 30 surrogates molecular weight, $MW_{i,j}$, required for C_{OA} calculations (see Section 3.3.3). A single $C\#_{i,j}$ value is calculated per chemical class, based on the average $C\#_j^{VOC}$ of the respective precursor class, and considering $C\#_{i,j} = C\#_j^{VOC} - \Delta C$, where

ΔC is the average loss in carbon due to fragmentation during the oxidation of precursors from all classes. ΔC is determined by systematically changing its value in multiple model runs and selecting the value that explains best the observed O:C ratios (see Fig. 8b). Likewise, a single $H\#_{i,j}$ value is assumed per chemical class, considering that $H\#_j/C\#_j$ equals $H\#_j^{VOC}/C\#_j^{VOC}$. Finally, $O\#_{i,j}$ is constrained by the $C\#_j$ and the surrogate volatility ($C_{i,j}^*$) based on the simplification of the SIMPOL model (Pankow and Asher, 2008), provided by Eq. (3) in Donahue et al. (2011). Based on this relationship, $O\#_{i,j}$ increases with decreasing $C\#_j$ and $C_{i,j}^*$. The O:C ratio of primary emissions is constrained in the model to the measured O:C in the beginning of each experiment, by setting $C\#^{OM_p}$ and calculating $O\#_i^{OM_p}$ using the same methodology as for $O\#_{i,j}$. The resulting $C\#^{OM_p}$ and $O\#_i^{OM_p}$ and the corresponding primary organic matter molecular weight, $MW_i^{OM_p}$, as well as $C\#_j$, $O\#_{i,j}$, $H\#_j$ and $MW_{i,j}$ are reported in Table S4.

10 3.3.3 Model outputs

The model provides the $\gamma_{i,j}$ and $\Delta H_{vap\ i,j}$ parameters. To reduce the model's degree of freedom we consider a single ΔH_{vap} for all surrogates from different chemical classes in different volatility bins. $\gamma_{i,j}$ is considered to follow a kernel normal distribution as a function of $\log C^*$, $\gamma_{i,j} \sim N(\mu_j, \sigma)$, where μ_j is the median value of $\log C^*$ and σ is the standard deviation. This step (1) insures positive $\gamma_{i,j}$ parameters, (2) significantly reduces the model's degree of freedom and (3) allows constraining 15 the total concentration of surrogates from a certain chemical class: $\sum_i^m \gamma_{i,j} = 1$.

The set of $\gamma_{i,j}$ and $\Delta H_{vap\ i,j}$ parameters are determined by minimizing the sum of mean bias (MB) and the root mean square error (RMSE) between modelled mass concentrations of the particulate organic phase, C_{OA} , calculated using Eq. (6) and concentrations measured by the AMS.

$$C_{OA} = \sum_j^n \sum_i^m MW_{i,j} x_{i,j}|_p + MW_i^{OM_p} x_i^{OM_p}|_p \quad (6)$$

20

The model fitted to the measured C_{OA} was also validated by external AMS measurements of the O:C ratio determined through high resolution analysis. The modelled O:C ratio was calculated at every experimental time step as follows:

$$O:C = \frac{\sum_j^n \sum_i^m O\#_{i,j} x_{i,j}|_p + O\#_i^{OM_p} x_i^{OM_p}|_p}{\sum_j^n \sum_i^m C\#_{i,j} x_{i,j}|_p + C\#_i^{OM_p} x_i^{OM_p}|_p} \quad (7)$$

3.3.4 Model optimization

The model is optimized to determine the volatility distributions of the oxidation products from different precursor classes described by μ_j, σ and their temperature-dependence described by ΔH_{vap} , to best fit the observed OA concentrations. For the model optimization, we used a genetic algorithm (GA), a metaheuristic procedure inspired by the theory of natural selection in biology, including selection, crossover and mutation processes, to efficiently generate high-quality solutions to optimize problems (Goldberg et al., 2007; Mitchell, 1996). The GA is initiated with a population of randomly selected individual solutions. The performance of each of these solutions is evaluated by a fitness function, and the fitness values are used to select more optimized solutions, referred to as parents. The new generation of solutions (denoted children) are produced either by randomly changing a single parent (as mutation) or by combining the vector entries of a pair of parents (as crossover). The evolution process will be repeated until the termination criterion is reached, here maximum iteration time. In this study, a population of 50 different sets of model parameters (μ_j, σ and ΔH_{vap}) was considered for each GA generation. The sum of mean bias and RMSE between measured and modelled COA of the 14 experiments were used as fitness function to evaluate the solutions. We assume the termination criterion is reached if no improvement in the fitness occurs after 50 generations, with a maximum of 500 total iterations allowed. The GA calculations were performed using the package “GA” for R (Scrucca et al., 2017). A bootstrap method was then adopted to quantify the uncertainty in the constrained parameters.

4. Results and discussion

4.1 Comparison of primary emissions across experiments

A larger amount of primary OGs was emitted into the chamber in Set1, with concentrations ranging from 950 to 7860 $\mu\text{g m}^{-3}$, while in Set2 the primary OGs concentrations ranged from 300 to 1360 $\mu\text{g m}^{-3}$. In the same way, the measured OA at the beginning of each test (POA) ranged from 10 to 180 $\mu\text{g m}^{-3}$ and from 9 to 22 $\mu\text{g m}^{-3}$ for Set1 and Set2, respectively (Table 1). The OGs composition for Set1 and Set2 is summarized in Fig. 2 showing the mean PTR-ToF-MS mass spectra (Fig. 2a, b), the relative contributions of the different compounds for different datasets (Fig. 2c) and the variability in composition among all experiments (Fig. 2d). Set1 shows higher relative contributions of furans and OVOC_{c<6} (Fig. 2a), while the contributions of PAH, SAH and OxyAH are higher in Set2 (Fig. 2b). The OxyAH compounds, mainly methyl and methoxy-phenols, are produced by lignin pyrolysis (Fine et al., 2001) while furans are formed from cellulose pyrolysis (Mettler et al., 2012). The chemical class referred to as ‘Others’ comprise compounds that do not show a clear decay upon oxidation and are therefore not considered as SOA precursors in the following analysis. ‘Others’ is dominated by acetic acid, previously reported as a major species in residential wood burning emissions (Bhattu et al., 2019). The majority of the compounds differ among datasets and the most significant difference estimated through the p value (probability associated with a student t -test) occurs for the OVOC_{c<6}, which is about a factor of 6 higher than the significance threshold ($p = 0.05$) for Set1. In order to investigate the similarity between all experiments a Spearman correlation matrix was calculated. Experiments from Set1 appear to be

consistently similar to each other while the experiments from Set2 are significantly different among each other in terms of composition of the primary emissions. A possible reason for such discrepancy was the difficulty in injecting flaming emissions without any significant smoldering contribution for Set2. This hypothesis is supported by the strong similarity between precursor compounds measured in some experiments supposed to represent flaming phase emissions only but apparently included some smoldering as well (9, 12, 13) with experiments from Set1 (1-7). Figure S2 reports the relative contributions of primary OGs (before photo-oxidation) for all compound classes for the fourteen experiments. Note that these trends are not correlated with the modified combustion efficiency (MCE), reported in Table 1, defined as $\text{CO}_2/(\text{CO}+\text{CO}_2)$, which was constant at 0.97 g g^{-1} , for Set2, but ranged from 0.8 g g^{-1} to 0.91 g g^{-1} for Set1.

Figure 3 shows the contribution of each class of precursor compounds and of the primary semi-volatile organic matter (OM_p) to the total primary emissions. OM_p is the total organic matter in the semi-volatile and low-volatility range in the particle and the gas phase (saturation concentration $< 1000 \mu\text{g m}^{-3}$ at 298 K) (see Section 3.3.2). Overall, the highest average relative contributions are related to $\text{OVOC}_{c<6}$ followed by furans and OxyAH but we also note an average large contribution by SAH for Set2. The two sets of experiments investigated clearly show different primary composition of emissions in terms of dominant contributions; in Set1 $\text{OVOC}_{c<6}$ and OxyAH dominate by far the total primary emissions while in Set2 the main species influencing the total primary emissions are OxyAH, $\text{OVOC}_{c<6}$ and SAH with roughly similar contribution (see Fig. 3b). Moreover, the calculated averaged OM_p/OGs ratios are around 0.05 and 0.03 for Set2 and Set1, respectively.

OGs undergo oxidation during atmospheric aging to form a complex mixture of products, some of which remain in the gas phase while others have sufficiently low volatility to partition to the particle phase. The consumption of the different OG classes over time is shown in Fig. 4a, b for Set1 and Set2 respectively. The general trends manifest that PAH and OxyAH are the most reactive classes, exhibiting an average consumption of up to 80% at the end of the experiments (after ~ 4 hours of aging) while for both the datasets SAH appears to be the least reactive class (with an average consumption between 10 and 20% at the end of experiments). Relevant compounds in the latter class are benzene (C_6H_6), toluene (C_7H_8) and xylene (C_8H_{10}), their slow reactivity is consistent with literature reaction rate constants toward OH, from the NIST database (NIST chemistry WebBook, 2018), of 1.22×10^{-12} , 6.13×10^{-12} and $7.51 \times 10^{-12} (\text{cm}^3 \text{ molec}^{-1} \text{ s}^{-1})$, respectively.

The two datasets differ for the OH dose; we observe in Set2 (Expt. 8-14) an overall higher consumption of all precursor classes due to the higher OH dose (representing a longer aging time in an ambient atmosphere). PAH shows the highest reactivity followed by OxyAH while for Set1 (Expt. 1-7) the fastest class of compounds to react is the OxyAH followed by PAH and $\text{OVOC}_{c<6}$. Moreover, despite of the lower OH exposure reached for Set1 the consumption of OxyAH and furans is substantially higher at comparable exposure levels.

In the same way, we also observe a higher SOA production for Set1 compared to Set2 at comparable OH exposure. The SOA/POA ranges between 2 and 6, similar to ratios observed in previous studies (Heringa et al., 2011a, Bruns et al., 2015, Grieshop et al., 2009, Tiitta et al., 2016).

Overall the same chemical classes appear to behave differently across the different sets of experiments. Such an inconsistency in behavior is either due to differences in the chemical composition within the same class or due to additional reactivity occurring in Set1.

To investigate the chemical differences within the same class of compounds across different experiments, Table 2 reports the 5 average reaction rate constants against OH of the different chemical classes calculated at the beginning of each experiment following Eq. (8).

$$\bar{k}_{OH,j,k} = \sum_i k_{OH,c,j} \times \frac{OG_{c,j,k}}{OG_{j,k}} \quad (8)$$

Here, c represents the single compound, j the family and k the experiment. k_{OH} is the reaction rate constant toward OH and OG 10 refers to the primary OGs.

OH reaction rate constants ($k_{OH,c,j}$) for each compound were calculated from Set2 only (Fig. 5), whereas the decay of the precursors contributing most to SOA formation during aging was compared with the expected decay based on literature. The good agreement indicates that for these experiments the consumption of the precursors was dominated by OH (Bruns et al. 2017). The average OH reaction rate constants ($\bar{k}_{OH,c,j}$) are reported in Table S3. They are determined for each precursor class

15 and calculated with a first order exponential fitting on the precursors' decay curves previously corrected for dilution.

The average reaction rate constants per family ($\bar{k}_{OH,j,k}$) are similar among the same families for different experiments suggesting that the variable behavior of the chemical classes across different experiments was due to differences in the reactive environment rather than a different chemical composition within a given class.

As introduced in Section 3.1.3, the total measured decay of OGs in Set1 could not be fully explained by dilution and reactivity 20 against OH, suggesting the presence of an additional loss process. To assess the remaining oxidation processes, k_{OH} values were used to estimate the missing loss process for Set1 according to Eq. (1). In this way the consumed fraction due to OH chemistry, dilution in the chamber and the additional reactivity was calculated for each OG compound family and is shown in Fig. 6. The additional reactivity appears to contribute to the total precursor consumption for most of the classes, with particular relevance for the OxyAH and PAH classes. This is in contrast with the calculated loss for the Set2 (Fig. S3) where the dominant 25 consumption is due to OH.

One possible hypothesis is that the remaining loss process might be due to reaction with the nitrate radical (NO_3), which absorbs in the visible region (~500-650 nm) and thus is not efficiently photolyzed by the black lights used here (Reed et al., 2016). Fig. S4 shows that for Set1 the NO_3 reaction rate constants (k_{NO_3}) for compounds found in the NIST database (NIST chemistry WebBook, 2018) (see Table S1) are well correlated with the amount reacted, making nitrate chemistry a likely loss 30 process (Schwantes et al., 2018). We note that while the OH production rate in the chamber is similar for the two sets of experiments, given the same injection rate of HONO, the OH total reactivity is significantly higher for Set 1, because of the

injection of ~ 5 times higher OG concentrations. As a result, the OH concentration is around 1.5×10^6 versus 10×10^6 molec cm^{-3} for Set1 and Set2, respectively, increasing the availability of OGs for consumption by other processes during Set1.

4.2 Model evaluation

As previously mentioned, the reaction of the OGs produces oxidation products (CG, condensable gases) which can 5 consequently partition between the gas and particle phases. Their concentration, estimated by accounting for the production minus the loss in the chamber, as described in Eq. (1), was used as input for the box model with the volatility basis set (VBS) scheme. Figure S5 shows the volatility distributions of different precursor classes for Set1 and Set2 to assess the influence of different processes occurring in different experiments.

We note that for Set1 the lower volatility bins exhibit higher contributions compared to Set2 but still within two standard 10 deviations, such that it is difficult to distinguish statistically different yields for most of the cases. Hence, the total volatility distribution was used to calculate the mass yield instead of a specific one for each dataset (Fig. 9). Mass yields calculated for the specific datasets Set1 and Set2 are reported in Fig. S6.

Fig. 7 shows the modelled and measured OA mass for all fourteen experiments, where Set1 accounts for both OH and NO_3 15 chemistry while Set2 includes OH chemistry only. The modelled OA is divided into POA and 6 SOA classes attributed to the respective precursor classes. Overall, the model performance is satisfactory, although in general the final OA concentration is slightly overpredicted while the initial production rate is underpredicted. Most of the SOA is attributed to furans (30.8%), OxyAH (19%) and $\text{OVOC}_{c<6}$ (12.5%) for Set1 while for Set2 there is a generally lower contribution from $\text{OVOC}_{c\geq 6}$ (7.8%) and a higher contribution from PAH (12%), especially for experiments 08, 13 and 14. The mean bias between measured and modelled OA averaged over all experiments is $-7.2 \mu\text{g m}^{-3}$ which corresponds to $\sim 15\%$ on average.

20 4.3 Investigation of OA chemical and physical properties

Comparisons between measured and modelled O:C ratios are reported in Fig. 8. The oxidation products elemental composition based on which the modelled O:C ratio is calculated are presented in Table S4. The oxidation products' carbon numbers that explained best the observed O:C ratio corresponds to a set ΔC of 0.6 (Fig. S7). There is a general increase in the O:C ratio 25 with time. Model and observations match in terms of average O:C ratio for each experiment but the temporal evolution of the ratio is not well predicted suggesting that there are additional processes that are not taken into account in the model. As the model was initiated using the measured POA O:C ratio at OH exposure equal to zero, an agreement between model and measurements can be observed at this time of the experiment. We do not find any systematic correlation of the bias with chamber conditions except for lower concentrations where experiments exhibit higher O:C ratios at the end. Overall for 30 experiments conducted at lower temperature (-10°C) the model tends to overestimate the O:C while for higher temperature experiments (15°C) the model clearly under-predicts the ratio upon aging especially at the end of the experiments indicating the presence of compounds with a higher number of oxygen (lower number of carbon) than predicted.

Fig. 9 shows mass yield curves for each class of compounds, in comparison with mass yields of several single compounds from literature (Table S2). The single compounds were selected according to their presence in the current study and compared to the respective chemical family. The reported published yields were discriminated according to experimental NO_x regimes, as low NO_x conditions generally lead to higher OA yields. Our study is more likely representative of a high NO_x regime and thus assesses the SOA forming potential for this atmospherically relevant condition. For the model and measurement conditions (C_{OA}~20-600 $\mu\text{g m}^{-3}$) the following median mass yields ranges were found: 7-20% for furans, 10-25% for SAH, 14-32% for PAH, 9-24% for OxyAH, 23-46% for OVOC_{c≥6} and 6-18% for OVOC_{c<6}. Mass yields were also calculated for the two separate datasets and reported in Fig. S6 in order to assess differences driven by specific combustion regimes. Considering ambient relevant conditions of C_{OA}~50 $\mu\text{g m}^{-3}$ we note a generally good agreement between the two datasets except for OxyAH which exhibit higher median yields (representing smoldering phase) of ~25% in Set1 and only ~10% in Set2 (representing flaming phase). Set2 on the other hand exhibited higher median yields for the OVOC_{c≥6} family (~20% compared to ~16 % for Set1).

The effect of temperature and OH exposure on OA concentrations and yields are shown in Fig. 10 for different primary OM loads (total primary gaseous and particulate OM_p + OGs) of 6, 60 and 600 $\mu\text{g m}^{-3}$. The range of temperatures investigated varies between 255 and 315 K. We find a general increase in total OA concentration with increasing OH exposure, decreasing experimental temperature, and higher initial loads, as expected. The average increase in OA concentration is 0.001, 0.03 and 0.6 $\mu\text{g m}^{-3} \text{ K}^{-1}$ for 6, 60 and 600 $\mu\text{g m}^{-3}$, respectively. Concerning SOA yields the temperature effect is also a function of OH exposure and aerosol load; SOA yields increase by 0.0001, 0.0006 and 0.002 $\text{g g}^{-1} \text{ K}^{-1}$ on average for 6, 60 and 600 $\mu\text{g m}^{-3}$, respectively, with a higher effect predicted at lower temperature. We note overall an average yield increase by a factor of 3-4 for a 10-fold increase in the primary OM loads at the highest OH exposure considered (8×10^7 molec $\text{cm}^{-3} \text{ h}$). Set2 exhibits higher yields because of lower contributions from the OVOC_{c<6} family, which does not produce significant amounts of SOA. SOA yields increase with increasing C_{OA} due to additional partitioning but also due to changes in the chemical composition and volatility of SOA species since they age differently with different experimental temperature and concentrations. Compounds with different oxygen to carbon ratios lead to different functionality, polarity and vapor pressure upon aging. Moreover, different temperatures result in different evaporation enthalpies that influence consequently the compounds' volatility and lifetime. The modeled SOA ΔH_{vap} for each family of precursors results to be 17.5 kJ mol^{-1} after GA calculation. This value is within the ranges of values reported in literature, where values between 11 and 44 kJ mol^{-1} were reported for biogenic and anthropogenic SOA precursors depending upon the reactant hydrocarbon mixture and NO_x concentration. For SOA formed both from α -pinene or toluene, a negative correlation between ΔH_{vap} and NO_x concentration was observed (Offenberg et al., 2006).

The modelled fractional contributions of the six different precursor classes to SOA are shown in Fig. 11 for Set1 and Set2. The most dominant contribution is from the OxyAH family apart from Set1 at high OH exposure where the contributions from precursors with higher volatility (furans and OVOC_{c<6}) are more strongly temperature-dependent. In detail, the OVOC_{c<6} family exhibits higher contribution with higher initial load and higher OH exposure. The SAH and PAH families have relevant

contributions for Set2 because these compounds are strongly emitted during the flaming phase. Since the SAH family consists of compounds that are less reactive than other families, they become relevant just at high OH exposure, while the compounds in the PAH family react faster and show a decreasing contribution with increasing OH exposure.

5. Conclusions

5 We performed box model simulations, based on the volatility basis set (VBS) approach, of residential wood combustion smog chamber experiments conducted at different temperatures, different combustion conditions and using different residential stoves. Primary emissions of SOA precursor compounds (OGs) and organic aerosol (OA) as well as their evolution during aging in the smog chamber were simultaneously monitored by a PTR-ToF-MS and an HR-ToF-AMS, respectively. This 10 enabled the identification of the nature of SOA precursors lumped into different classes according to their chemical composition.

The knowledge about the nature of SOA precursors was used to better constrain model parameters, in the oxidation products production rates and elemental composition. Using the measured OA mass, we were able to determine the volatility distributions and ΔH_{vap} for the products formed from the oxidation of the dominant precursor compound classes. We estimated the contributions of different compound classes to SOA and evaluate how the variability in the emission composition under a 15 wide range of conditions would influence the SOA yield predictions. Investigation of different experimental temperatures allowed the evaluation of the model evaporation enthalpies which have a decisive influence on the volatility of the emissions and hence their atmospheric lifetimes. Upon aging, compounds with lower atomic O:C ratios are converted through the oxidation pathway to products with higher functionality, higher polarity and lower vapor pressure. As a result, a part of these 20 products (re-)condense to the particle phase with partial pressures determined by their volatility, ambient temperature and concentration of the particulate organic mixture. While the degree of oxygenation increases during aging, organic species may also fragment into more volatile compounds, being eventually converted into CO₂. Understanding the balance between oxygenation and fragmentation, their effect on volatility of emissions and timescale of these processes is essential to predict the evolution of the OA concentration.

Overall we developed a framework useful to constrain complex emissions and suitable for sophisticated mass spectrometry 25 analysis with the novelty and ability of identifying the contributions of different classes of OG precursors to SOA formation. The main focus of the study included the investigation of smoldering versus flaming emissions, resulting in predominant contributions of different classes of compounds according to the combustion phase investigated. Smoldering phase emissions were dominated by the OVOC_{<6} compound family while the flaming phase exhibited higher contributions by the SAH and PAH families. For both phases, SOA formation is found to be dominated by OxyAH (e.g. phenols and cresols), emitted from 30 lignin pyrolysis. These species were therefore predicted to be important markers to be monitored in air pollution studies in order to estimate the SOA forming potential from real emissions.

Appendix A

In this appendix, we present the derivation of the thermodynamic equations used in the model. We considered the species in the gas and the particle phase to be permanently at equilibrium, as condensation is expected to be faster than oxidation (time scales for oxidized vapours condensation < 1 minute assuming no particle phase diffusion limitations, Bertrand et al., 2018b).

5 Accordingly, the relation between the aerosol and gas phase activities satisfies the following expression:

$$x_{i,j}|_g = \gamma_{i,j} \chi_{i,j} x_{i,j}^0 \quad (\text{A1})$$

Here, $x_{i,j}|_g$ denotes the gas phase molar concentration of a surrogate in a volatility bin i formed from a precursor class j . The product $\gamma_{i,j} \chi_{i,j}$ represents the activity of the same surrogate in the particle phase, where $\gamma_{i,j}$ and $\chi_{i,j}$ are the activity coefficient and the fraction of the surrogate in the particle phase, respectively. $x_{i,j}^0$ is the equilibrium molar saturation concentration of the pure surrogate, related to its equilibrium vapor pressure, $p_{i,j}^0$, according to Eq. (A2).

$$x_{i,j}^0 = \frac{p_{i,j}^0}{RT} \quad (\text{A2})$$

Here, R and T are the ideal gas constant and the temperature, respectively. The effective molar saturation concentration ($x_{i,j}^*$) which takes into account the influence of non-ideal mixing on the compounds' activity, can be defined as the product of $\gamma_{i,j}$ and $x_{i,j}^0$:

$$x_{i,j}^* = \gamma_{i,j} x_{i,j}^0 \quad (\text{A3})$$

Similar to $p_{i,j}^0$, $x_{i,j}^*$ can be written as a function of temperature, according to the Clausius-Clapeyron relationship based on Eq. (A4).

$$\ln\left(\frac{x_{i,j}^*(T)}{x_{i,j}^*(T_{ref})}\right) = -\frac{\Delta H_{vap\,i,j}}{R} \left(\frac{1}{T} - \frac{1}{T_{ref}}\right) \quad (\text{A4})$$

20

Here, T and T_{ref} are the experimental and reference ($T_{ref} = 298\text{K}$) temperatures, respectively. $\Delta H_{vap\,i,j}$ is the effective enthalpy of evaporation. It includes the effects of temperature on (1) the pure compound vapor pressure ($p_{i,j}^0$), (2) the compounds' mixing properties in the condensed phase, i.e. $\gamma_{i,j}$ and (3) the radical chemistry reaction rate constants and branching ratios in the gas-phase (Stolzenburg et al., 2018).

25 $x_{i,j}^*$ is related to the Donahue effective mass saturation concentration (Donahue et al., 2012), $C_{i,j}^*$, which is the inverse of the Pankow equilibrium constant (Pankow, 1987), through the compounds' molecular weight, $MW_{i,j}$, as indicated in Eq. (A5).

$$C_{i,j}^* = MW_{i,j} x_{i,j}^* \quad (\text{A5})$$

To constrain the model to the measurements, it is of convenience to rearrange Eq. (A1) and (A3) as a function of the surrogate total concentration, $x_{i,j}|_{g+p} = x_{i,j}|_g + x_{i,j}|_p$ and the total molar concentration of species in the particle phase (x_{OA}) which 5 yields the following expression:

$$x_{i,j}|_p = \left(1 + \frac{x_{i,j}^*}{x_{OA}}\right)^{-1} x_{i,j}|_{g+p} \quad (\text{A6})$$

The parameters in Eq. (A6) were equated as follows:

- The modelled molar concentration of the particulate organic phase was expressed as the sum of the concentration of all surrogates in the particle phase Eq. (A7).

10

$$x_{OA} = \sum_j^n \sum_i^m x_{i,j}|_p + x_i^{OM_p}|_p \quad (\text{A7})$$

Here, m and n are the total number of volatility bins and precursors chemical classes, respectively. $x_i^{OM_p}|_p$ is the particle phase molar concentration of primary organic matter in volatility bin i . The $x_i^{OM_p}|_p$ is calculated based on 15 $x_i^{OM_p}|_{g+p}$ in both phases, following a similar computation as for SOA (Eq. A6). $x_i^{OM_p}|_{g+p}$ was inferred from the measured POA concentrations injected into the chamber at the beginning of the experiment and using the volatility distribution function of wood combustion emissions in May et al. (2013).

15

- $x_{i,j}|_{g+p}$ was derived from the precursor oxidation rates measured by the PTR-ToF-MS. The change in the total concentration of oxidation products from a precursor class j in both gas and particle phases, $x_j|_{g+p}$, was expressed as 20 follows:

$$\frac{dx_j|_{g+p}}{dt} = k_{OH} * [OH] * [\text{OG}_j] + k_{other} * [\text{OG}_j] - k_{dil} * x_j|_{g+p} \quad (\text{A8})$$

Here, $[\text{OG}_j]$ is the molar concentration of total OG precursors in class j . For the definition of the other parameters, the reader is referred to Eq. (1). $x_j|_{g+p}$ is calculated by numerically integrating Eq. (A8). $x_j|_{g+p}$ is related to the 25 concentration of the different surrogates from a precursor class j in different volatility bins, $x_{i,j}|_{g+p}$ (Eq. A6), through their yields, $Y_{i,j}$:

$$x_{i,j}|_{g+p} = Y_{i,j}x_j|_{g+p} \quad (\text{A9})$$

These yields, which represent the surrogate volatility distributions were determined by the model.

5

Authors contribution

Main author: GS. Conceptualization: IEH, JGS, NM, ASHP. Experimental work: GS, AB, EB, SP. Formal analysis: GS, IEH, AB, EB. Model development and output analysis: JJ, IEH, SA. Supervision: JGS, IEH, ASHP, UB. Writing: All.

10

Acknowledgments

This study was supported by the Swiss National Science Foundation (project WOOSHI (200021L_140590) and SNSF Starting Grant IPR-SHOP (BSSGI0_155846)), the European Community's Seventh Framework Programme (FP7/2007-2013) under grant agreement no. 290605 (PSI-FELLOW), the European Union's Horizon 2020 research and innovation programme through
15 the EUROCHAMP-2020 Infrastructure Activity under grant agreement no. 730997, and the Competence Centers Environment and Sustainability (CCES) and Energy and Mobility (CCEM) (project OPTIWARES). AMU acknowledges support from the French Environment and Energy Management Agency (ADEME) under the grant 1562C0019 (VULCAIN project) and the Provence-Alpes-Côte d'Azur (PACA) region. We appreciate the availability of the VBS framework in CAMx and support of RAMBOLL.

20

References

Aiken, A. C., DeCarlo, P. F., Kroll, J. H., Worsnop, D. R., Huffman, J. A., Docherty, K. S., Ulbrich, I. M., Mohr, C., Kimmel, J. R., Sueper, D., Sun, Y., Zhang, Q., Trimborn, A., Northway, M., Ziemann, P. J., Canagaratna, M. R., Onasch, T. B., Alfarra,

M. R., Prevot, A. S. H., Dommen, J., Duplissy, J., Metzger, A., Baltensperger, U. and Jimenez, J. L.: O/C and OM/OC ratios of primary, secondary, and ambient organic aerosols with high-resolution time-of-flight aerosol mass spectrometry, *Environmental Science & Technology*, 42(12), 4478–4485, doi:10.1021/es703009q, 2008.

Atkinson, R. and Arey, J.: Atmospheric degradation of volatile organic compounds, *Chemical Reviews*, 103(12), 4605–4638, 5 doi:10.1021/cr0206420, 2003.

Barmet, P., Dommen, J., DeCarlo, P. F., Tritscher, T., Praplan, A. P., Platt, S. M., Prévôt, A. S. H., Donahue, N. M. and Baltensperger, U.: OH clock determination by proton transfer reaction mass spectrometry at an environmental chamber, *Atmos. Meas. Tech.*, 5(3), 647–656, doi:10.5194/amt-5-647-2012, 2012.

Bhattu, D., Zotter, P., Zhou, J., Stefenelli, G., Klein, F., Bertrand, A., Temime-Roussel, B., Marchand, N., Slowik, J. G., 10 Baltensperger, U., Prévôt, A. S. H., Nussbaumer, T., El Haddad, I. and Dommen, J.: Effect of stove technology and combustion conditions on gas and particulate emissions from residential biomass combustion, *Env. Sci Technol*, 53(4), 2209–2219, doi:10.1021/acs.est.8b05020, 2019.

Bertrand, A., Stefenelli, G., Bruns, E. A., Pieber, S. M., Temime-Roussel, B., Slowik, J. G., Prévôt, A. S. H., Wortham, H., El Haddad, I. and Marchand, N.: Primary emissions and secondary aerosol production potential from woodstoves for residential 15 heating: Influence of the stove technology and combustion efficiency, *Atmos. Environ.*, 169, 65–79, doi:10.1016/j.atmosenv.2017.09.005, 2017.

Bertrand, A., Stefenelli, G., Jen, C. N., Pieber, S. M., Bruns, E. A., Ni, H., Temime-Roussel, B., Slowik, J. G., Goldstein, A. H., El Haddad, I., Baltensperger, U., Prévôt, A. S. H., Wortham, H. and Marchand, N.: Evolution of the chemical fingerprint of biomass burning organic aerosol during aging, *Atmos. Chem. Phys.*, 18(10), 7607–7624, doi:10.5194/acp-18-7607-2018, 20 2018a.

Bertrand, A., Stefenelli, G., Pieber, S. M., Bruns, E. A., Temime-Roussel, B., Slowik, J. G., Wortham, H., Prévôt, A. S. H., El Haddad, I. and Marchand, N.: Influence of the vapor wall loss on the degradation rate constants in chamber experiments of levoglucosan and other biomass burning markers, *Atmos. Chem. Phys.*, 18(15), 10915–10930, doi:10.5194/acp-18-10915- 2018, 2018b.

Bian, Q., Jathar, S. H., Kodros, J. K., Barsanti, K. C., Hatch, L. E., May, A. A., Kreidenweis, S. M. and Pierce, J. R.: Secondary 25 organic aerosol formation in biomass-burning plumes: theoretical analysis of lab studies and ambient plumes, *Atmos. Chem. Phys.*, 17(8), 5459–5475, doi:10.5194/acp-17-5459-2017, 2017.

Bozzetti, C., Sosedova, Y., Xiao, M., Daellenbach, K. R., Ulevicius, V., Dudoit, V., Mordas, G., Byčenkiė, S., Plauškaitė, K., Vlachou, A., Golly, B., Chazeau, B., Besombes, J.-L., Baltensperger, U., Jaffrezo, J.-L., Slowik, J. G., El Haddad, I. and 30 Prévôt, A. S. H.: Argon offline-AMS source apportionment of organic aerosol over yearly cycles for an urban, rural, and marine site in northern Europe, *Atmos. Chem. Phys.*, 17(1), 117–141, doi:10.5194/acp-17-117-2017, 2017.

Bruns, E. A., Krapf, M., Orasche, J., Huang, Y., Zimmermann, R., Drinovec, L., Močnik, G., El-Haddad, I., Slowik, J. G., Dommen, J., Baltensperger, U. and Prévôt, A. S. H.: Characterization of primary and secondary wood combustion products generated under different burner loads, *Atmos. Chem. Phys.*, 15(5), 2825–2841, doi:10.5194/acp-15-2825-2015, 2015.

Bruns, E. A., El Haddad, I., Slowik, J. G., Kilic, D., Klein, F., Baltensperger, U. and Prévôt, A. S. H.: Identification of significant precursor gases of secondary organic aerosols from residential wood combustion, *Sci. Rep-Uk*, 6(1), doi:10.1038/srep27881, 2016.

Bruns, E. A., Slowik, J. G., El Haddad, I., Kilic, D., Klein, F., Dommen, J., Temime-Roussel, B., Marchand, N., Baltensperger, U. and Prévôt, A. S. H.: Characterization of gas-phase organics using proton transfer reaction time-of-flight mass spectrometry: fresh and aged residential wood combustion emissions, *Atmospheric Chemistry and Physics*, 17(1), 705–720, doi:10.5194/acp-17-705-2017, 2017.

Cappellin, L., Karl, T., Probst, M., Ismailova, O., Winkler, P. M., Soukoulis, C., Aprea, E., Märk, T. D., Gasperi, F. and Biasioli, F.: On Quantitative determination of volatile organic compound concentrations using proton transfer reaction time-of-flight mass spectrometry, *Environ. Sci. Technol.*, 46(4), 2283–2290, doi:10.1021/es203985t, 2012.

Chen, J., Li, C., Ristovski, Z., Milic, A., Gu, Y., Islam, M. S., Wang, S., Hao, J., Zhang, H., He, C., Guo, H., Fu, H., Miljevic, B., Morawska, L., Thai, P., Lam, Y. F., Pereira, G., Ding, A., Huang, X. and Dumka, U. C.: A review of biomass burning: Emissions and impacts on air quality, health and climate in China, *Science of The Total Environment*, 579, 1000–1034, doi:10.1016/j.scitotenv.2016.11.025, 2017.

Ciarelli, G., El Haddad, I., Bruns, E., Aksoyoglu, S., Möhler, O., Baltensperger, U. and Prévôt, A. S. H.: Constraining a hybrid volatility basis-set model for aging of wood-burning emissions using smog chamber experiments: a box-model study based on the VBS scheme of the CAMx model (v5.40), *Geosci. Model Dev.*, 10(6), 2303–2320, doi:10.5194/gmd-10-2303-2017, 2017a.

Ciarelli, G., Aksoyoglu, S., El Haddad, I., Bruns, E. A., Crippa, M., Poulain, L., Äijälä, M., Carbone, S., Freney, E., Dowd, C., Baltensperger, U. and Prévôt, A. S. H.: Modelling winter organic aerosol at the European scale with CAMx: evaluation and source apportionment with a VBS parameterization based on novel wood burning smog chamber experiments, *Atmos. Chem. Phys.*, 17(12), 7653–7669, doi:10.5194/acp-17-7653-2017, 2017b.

Crippa, M., DeCarlo, P. F., Slowik, J. G., Mohr, C., Heringa, M. F., Chirico, R., Poulain, L., Freutel, F., Sciare, J., Cozic, J., Di Marco, C. F., Elsasser, M., Nicolas, J. B., Marchand, N., Abidi, E., Wiedensohler, A., Drewnick, F., Schneider, J., Borrmann, S., Nemitz, E., Zimmermann, R., Jaffrezo, J.-L., Prévôt, A. S. H. and Baltensperger, U.: Wintertime aerosol chemical composition and source apportionment of the organic fraction in the metropolitan area of Paris, *Atmos. Chem. Phys.*, 13(2), 961–981, doi:10.5194/acp-13-961-2013, 2013.

DeCarlo, P. F., Kimmel, J. R., Trimborn, A., Northway, M. J., Jayne, J. T., Aiken, A. C., Gonin, M., Fuhrer, K., Horvath, T., Docherty, K. S., Worsnop, D. R. and Jimenez, J. L.: Field-deployable, high-resolution, time-of-flight aerosol mass spectrometer, *Anal. Chem.*, 78(24), 8281–8289, doi:10.1021/ac061249n, 2006.

Donahue, N. M., Robinson, A. L., Stanier, C. O. and Pandis, S. N.: Coupled partitioning, dilution, and chemical aging of semivolatile organics, *Environ. Sci. Technol.*, 40(8), 2635–2643, doi:10.1021/es052297c, 2006.

Donahue, N. M., Robinson, A. L. and Pandis, S. N.: Atmospheric organic particulate matter: From smoke to secondary organic aerosol, *Atmos. Environ.*, 43(1), 94–106, doi:10.1016/j.atmosenv.2008.09.055, 2009.

Donahue, N. M., Epstein, S. A., Pandis, S. N. and Robinson, A. L.: A two-dimensional volatility basis set: 1. organic-aerosol mixing thermodynamics, *Atmos. Chem. Phys.*, 11(7), 3303–3318, doi:10.5194/acp-11-3303-2011, 2011.

Donahue, N. M., Robinson, A. L., Trump, E. R., Riipinen, I. and Kroll, J. H.: Volatility and aging of atmospheric organic aerosol, *Top. Curr. Chem.*, vol. 339, edited by V. F. McNeill and P. A. Ariya, pp. 97–143, Springer Berlin Heidelberg, Berlin, 5 Heidelberg., 2012.

Drinovec, L., Močnik, G., Zotter, P., Prévôt, A. S. H., Ruckstuhl, C., Coz, E., Rupakheti, M., Sciare, J., Müller, T., Wiedensohler, A. and Hansen, A. D. A.: The dual-spot Aethalometer: an improved measurement of aerosol black carbon with real-time loading compensation, *Atmos. Meas. Tech.*, 8(5), 1965–1979, doi:10.5194/amt-8-1965-2015, 2015.

Dzepina, K., Volkamer, R. M., Madronich, S., Tulet, P., Ulbrich, I. M., Zhang, Q., Cappa, C. D., Ziemann, P. J. and Jimenez, 10 J. L.: Evaluation of recently-proposed secondary organic aerosol models for a case study in Mexico City, *Atmos. Chem. Phys.*, 9(15), 5681–5709, doi:10.5194/acp-9-5681-2009, 2009.

Eriksson, A. C., Nordin, E. Z., Nyström, R., Pettersson, E., Swietlicki, E., Bergvall, C., Westerholm, R., Boman, C. and Pagels, J. H.: Particulate PAH emissions from residential biomass combustion: time-resolved analysis with aerosol mass spectrometry, *Environ. Sci. Technol.*, 48(12), 7143–7150, doi:10.1021/es500486j, 2014.

Fine, P. M., Cass, G. R. and Simoneit, B. R. T.: Chemical characterization of fine particle emissions from fireplace combustion of woods grown in the northeastern united states, *Environ. Sci. Technol.*, 35(13), 2665–2675, doi:10.1021/es001466k, 2001.

Fine, P. M., Cass, G. R. and Simoneit, B. R. T.: Chemical characterization of fine particle emissions from the fireplace combustion of woods grown in the southern united states, *Environ. Sci. Technol.*, 36(7), 1442–1451, doi:10.1021/es0108988, 2002.

Gentner, D. R., Jathar, S. H., Gordon, T. D., Bahreini, R., Day, D. A., El Haddad, I., Hayes, P. L., Pieber, S. M., Platt, S. M., de Gouw, J., Goldstein, A. H., Harley, R. A., Jimenez, J. L., Prévôt, A. S. H. and Robinson, A. L.: Review of urban secondary organic aerosol formation from gasoline and diesel motor vehicle emissions, *Environ. Sci. Technol.*, 51(3), 1074–1093, doi:10.1021/acs.est.6b04509, 2017.

Gobiet, A., Kotlarski, S., Beniston, M., Heinrich, G., Rajczak, J. and Stoffel, M.: 21st century climate change in the European 25 Alps—A review, *Science of The Total Environment*, 493, 1138–1151, doi:10.1016/j.scitotenv.2013.07.050, 2014.

Goldberg, D. E., Sastry, K. and Llorà, X.: Toward routine billion-variable optimization using genetic algorithms, *Complexity*, 12(3), 27–29, doi:10.1002/cplx.20168, 2007.

Gordon, T. D., Presto, A. A., May, A. A., Nguyen, N. T., Lipsky, E. M., Donahue, N. M., Gutierrez, A., Zhang, M., Maddox, C., Rieger, P., Chattopadhyay, S., Maldonado, H., Maricq, M. M. and Robinson, A. L.: Secondary organic aerosol formation 30 exceeds primary particulate matter emissions for light-duty gasoline vehicles, *Atmos. Chem. Phys.*, 14(9), 4661–4678, doi:10.5194/acp-14-4661-2014, 2014a.

Gordon, T. D., Presto, A. A., Nguyen, N. T., Robertson, W. H., Na, K., Sahay, K. N., Zhang, M., Maddox, C., Rieger, P. and Chattopadhyay, S.: Secondary organic aerosol production from diesel vehicle exhaust: impact of aftertreatment, fuel chemistry and driving cycle, *Atmos. Chem. Phys.*, 14(9), 4643–4659, 2014b.

Grieshop, A. P., Logue, J. M., Donahue, N. M. and Robinson, A. L.: Laboratory investigation of photochemical oxidation of organic aerosol from wood fires 1: measurement and simulation of organic aerosol evolution, *Atmos. Chem. Phys.*, 9(4), 1263–1277, doi:10.5194/acp-9-1263-2009, 2009.

Gueneron, M., Erickson, M. H., VanderSchelden, G. S. and Jobson, B. T.: PTR-MS fragmentation patterns of gasoline hydrocarbons, *Inter. J. Mass Spectrom.*, 379, 97–109, doi:10.1016/j.ijms.2015.01.001, 2015.

Heringa, M. F., DeCarlo, P. F., Chirico, R., Tritscher, T., Dommen, J., Weingartner, E., Richter, R., Wehrle, G., Prévôt, A. S. H. and Baltensperger, U.: Investigations of primary and secondary particulate matter of different wood combustion appliances with a high-resolution time-of-flight aerosol mass spectrometer, *Atmospheric Chem. Phys.*, 11(12), 5945–5957, doi:10.5194/acp-11-5945-2011, 2011.

Jathar, S. H., Farina, S. C., Robinson, A. L. and Adams, P. J.: The influence of semi-volatile and reactive primary emissions on the abundance and properties of global organic aerosol, *Atmos. Chem. Phys.*, 11(15), 7727–7746, doi:10.5194/acp-11-7727-2011, 2011.

Jathar, S. H., Miracolo, M. A., Presto, A. A., Donahue, N. M., Adams, P. J. and Robinson, A. L.: Modeling the formation and properties of traditional and non-traditional secondary organic aerosol: problem formulation and application to aircraft exhaust, *Atmos. Chem. Phys.*, 12(19), 9025–9040, doi:10.5194/acp-12-9025-2012, 2012.

Jathar, S. H., Miracolo, M. A., Tkacik, D. S., Donahue, N. M., Adams, P. J. and Robinson, A. L.: Secondary organic aerosol formation from photo-oxidation of unburned fuel: experimental results and implications for aerosol formation from combustion emissions, *Environ. Sci. Technol.*, 47(22), 12886–12893, doi:10.1021/es403445q, 2013.

Jathar, S. H., Donahue, N. M., Adams, P. J. and Robinson, A. L.: Testing secondary organic aerosol models using smog chamber data for complex precursor mixtures: influence of precursor volatility and molecular structure, *Atmos. Chem. Phys.*, 14(11), 5771–5780, doi:10.5194/acp-14-5771-2014, 2014a.

Jathar, S. H., Gordon, T. D., Hennigan, C. J., Pye, H. O. T., Pouliot, G., Adams, P. J., Donahue, N. M. and Robinson, A. L.: Unspeciated organic emissions from combustion sources and their influence on the secondary organic aerosol budget in the United States, *Proceedings of the National Academy of Sciences*, 111(29), 10473–10478, doi:10.1073/pnas.1323740111, 2014b.

Kılıç, D., El Haddad, I., Brem, B. T., Bruns, E., Bozetti, C., Corbin, J., Durdina, L., Huang, R.-J., Jiang, J., Klein, F., Lavi, A., Pieber, S. M., Rindlisbacher, T., Rudich, Y., Slowik, J. G., Wang, J., Baltensperger, U. and Prévôt, A. S. H.: Identification of secondary aerosol precursors emitted by an aircraft turbofan, *Atmos. Chem. Phys.*, 18(10), 7379–7391, doi:10.5194/acp-18-7379-2018, 2018.

Klein, F., Farren, N. J., Bozzetti, C., Daellenbach, K. R., Kilic, D., Kumar, N. K., Pieber, S. M., Slowik, J. G., Tuthill, R. N., Hamilton, J. F., Baltensperger, U., Prévôt, A. S. H. and El Haddad, I.: Indoor terpene emissions from cooking with herbs and pepper and their secondary organic aerosol production potential, *Sci. Rep.-Uk*, 6(1), doi:10.1038/srep36623, 2016.

Koppmann, R., von Czapiewski, K. and Reid, J. S.: A review of biomass burning emissions, part I: gaseous emissions of carbon monoxide, methane, volatile organic compounds, and nitrogen containing compounds, *Atmos. Chem. Phys. Discussions*, 5(5), 10455–10516, doi:10.5194/acpd-5-10455-2005, 2005.

Kumar, N. K., Corbin, J. C., Bruns, E. A., Massabó, D., Slowik, J. G., Drinovec, L., Močnik, G., Prati, P., Vlachou, A., Baltensperger, U., Gysel, M., El-Haddad, I. and Prévôt, A. S. H.: Production of particulate brown carbon during atmospheric aging of wood-burning emissions, *Atmos. Chem. Phys. Discussions*, 1–33, doi:10.5194/acp-2018-159, 2018.

Lanz, V. A., Prévôt, A. S. H., Alfarra, M. R., Weimer, S., Mohr, C., DeCarlo, P. F., Gianini, M. F. D., Hueglin, C., Schneider, J., Favez, O., D'Anna, B., George, C. and Baltensperger, U.: Characterization of aerosol chemical composition with aerosol mass spectrometry in Central Europe: an overview, *Atmos. Chem. Phys.*, 10(21), 10453–10471, doi:10.5194/acp-10-10453-10, 2010.

May, A. A., Levin, E. J. T., Hennigan, C. J., Riipinen, I., Lee, T., Collett, J. L., Jimenez, J. L., Kreidenweis, S. M. and Robinson, A. L.: Gas-particle partitioning of primary organic aerosol emissions: 3. Biomass burning: biomass-burning partitioning, *J. Geophys. Res.: Atmospheres*, 118(19), 11,327-11,338, doi:10.1002/jgrd.50828, 2013.

McDonald, J. D., Zielinska, B., Fujita, E. M., Sagebiel, J. C., Chow, J. C. and Watson, J. G.: Fine particle and gaseous emission rates from residential wood combustion, *Environ. Sci. Technol.*, 34(11), 2080–2091, doi:10.1021/es9909632, 2000.

Miracolo, M. A., Hennigan, C. J., Ranjan, M., Nguyen, N. T., Gordon, T. D., Lipsky, E. M., Presto, A. A., Donahue, N. M. and Robinson, A. L.: Secondary aerosol formation from photochemical aging of aircraft exhaust in a smog chamber, *Atmos. Chem. Phys.*, 11(9), 4135–4147, doi:10.5194/acp-11-4135-2011, 2011.

Mitchell, M.: An introduction to genetic algorithms, *Camb. Mass. Lond. Engl. Fifth Print.*, 3, 62–75, 1999.

Nah, T., McVay, R. C., Pierce, J. R., Seinfeld, J. H. and Ng, N. L.: Constraining uncertainties in particle-wall deposition correction during SOA formation in chamber experiments, *Atmos. Chem. Phys.*, 17(3), 2297–2310, doi:10.5194/acp-17-2297-2017, 2017.

NIST Chemistry WebBook, NIST Standard Reference Database Number 69, Eds. P.J. Linstrom and W.G. Mallard, National Institute of Standards and Technology, Gaithersburg MD, 20899, <https://doi.org/10.18434/T4D303>, (retrieved November 29, 2018).

Nolte, C. G., Schauer, J. J., Cass, G. R. and Simoneit, B. R. T.: Highly polar organic compounds present in wood smoke and in the ambient atmosphere, *environ. Sci. Technol.*, 35(10), 1912–1919, doi:10.1021/es001420r, 2001.

Offenberg, J. H., Kleindienst, T. E., Jaoui, M., Lewandowski, M. and Edney, E. O.: Thermal properties of secondary organic aerosols, *Geophysical Research Letters*, 33(3), doi:10.1029/2005GL024623, 2006.

Pandis, S. N., Donahue, N. M., Murphy, B. N., Riipinen, I., Fountoukis, C., Karnezi, E., Patoulias, D. and Skyllakou, K.: Introductory lecture: Atmospheric organic aerosols: insights from the combination of measurements and chemical transport models, *Faraday Discussions*, 165, 9, doi:10.1039/c3fd00108c, 2013.

Pankow, J. F.: Review and comparative analysis of the theories on partitioning between the gas and aerosol particulate phases in the atmosphere, *Atmos. Environ.* (1967), 21(11), 2275–2283, doi:10.1016/0004-6981(87)90363-5, 1987.

Pankow, J. F. and Asher, W. E.: SIMPOL.1: a simple group contribution method for predicting vapor pressures and enthalpies of vaporization of multifunctional organic compounds, *Atmos. Chem. Phys.*, 24, 2008.

Pettersson, E., Boman, C., Westerholm, R., Boström, D. and Nordin, A.: Stove performance and emission characteristics in residential wood log and pellet combustion, Part 2. Wood Stove, *Energy & Fuels*, 25(1), 315–323, doi:10.1021/ef1007787, 5 2011.

Platt, S. M., El Haddad, I., Zardini, A. A., Clairotte, M., Astorga, C., Wolf, R., Slowik, J. G., Temime-Roussel, B., Marchand, N., Ježek, I., Drinovec, L., Močnik, G., Möhler, O., Richter, R., Barmet, P., Bianchi, F., Baltensperger, U. and Prévôt, A. S. H.: Secondary organic aerosol formation from gasoline vehicle emissions in a new mobile environmental reaction chamber, *Atmos. Chem. Phys.*, 13(18), 9141–9158, doi:10.5194/acp-13-9141-2013, 2013.

10 Platt, S. M., El Haddad, I., Pieber, S. M., Zardini, A. A., Suarez-Bertoa, R., Clairotte, M., Daellenbach, K. R., Huang, R.-J., Slowik, J. G., Hellebust, S., Temime-Roussel, B., Marchand, N., de Gouw, J., Jimenez, J. L., Hayes, P. L., Robinson, A. L., Baltensperger, U., Astorga, C. and Prévôt, A. S. H.: Gasoline cars produce more carbonaceous particulate matter than modern filter-equipped diesel cars, *Sci. Rep.-Uk*, 7(1), doi:10.1038/s41598-017-03714-9, 2017.

Pye, H. O. T. and Seinfeld, J. H.: A global perspective on aerosol from low-volatility organic compounds, *Atmos. Chem. 15 Phys.*, 25, 2010.

Pieber, S. M., Kumar, N. K., Klein, F., Comte, P., Bhattu, D., Dommen, J., Bruns, E. A., Kılıç, D., El Haddad, I., Keller, A., Czerwinski, J., Heeb, N., Baltensperger, U., Slowik, J. G. and Prévôt, A. S. H.: Gas-phase composition and secondary organic aerosol formation from standard and particle filter-retrofitted gasoline direct injection vehicles investigated in a batch and flow reactor, *Atmos. Chem. Phys.*, 18(13), 9929–9954, doi:10.5194/acp-18-9929-2018, 2018.

20 Reda, A. A., Czech, H., Schnelle-Kreis, J., Sippula, O., Orasche, J., Weggler, B., Abbaszade, G., Arteaga-Salas, J. M., Kortelainen, M., Tissari, J., Jokiniemi, J., Streibel, T. and Zimmermann, R.: Analysis of gas-phase carbonyl compounds in emissions from modern wood combustion appliances: influence of wood type and combustion appliance, *Energy & Fuels*, 29(6), 3897–3907, doi:10.1021/ef502877c, 2015.

Reed, C., Evans, M. J., Di Carlo, P., Lee, J. D. and Carpenter, L. J.: Interferences in photolytic NO₂ measurements: explanation 25 for an apparent missing oxidant. *Atmos. Chem. Phys.*, 16(7), 4707–4724, doi:10.5194/acp-16-4707-2016, 2016.

Robinson, A. L., Donahue, N. M., Shrivastava, M. K., Weitkamp, E. A., Sage, A. M., Grieshop, A. P., Lane, T. E., Pierce, J. R. and Pandis, S. N.: Rethinking organic aerosols: semivolatile emissions and photochemical aging, *Science*, 315(5816), 1259–1262, doi:10.1126/science.1133061, 2007.

30 Robinson, A. L., Grieshop, A. P., Donahue, N. M. and Hunt, S. W.: Updating the conceptual model for fine particle mass emissions from combustion systems. *Japca J. Air. Waste Ma.*, 60(10), 1204–1222, doi:10.3155/1047-3289.60.10.1204, 2010.

Schauer, J. J., Kleeman, M. J., Cass, G. R. and Simoneit, B. R. T.: Measurement of emissions from air pollution sources. 2. C₁ through C₃₀ organic compounds from medium duty diesel trucks, *Environ. Sci. Technol.*, 33(10), 1578–1587, doi:10.1021/es980081n, 1999.

Schauer, J. J., Kleeman, M. J., Cass, G. R. and Simoneit, B. R. T.: Measurement of emissions from air pollution sources. 3. C1 – C29 organic compounds from fireplace combustion of wood, *Environ. Sci. Technol.*, 35(9), 1716–1728, doi:10.1021/es001331e, 2001.

Schwantes, R. H., Schilling, K. A., McVay, R. C., Lignell, H., Coggon, M. M., Zhang, X., Wennberg, P. O. and Seinfeld, J. H.: Formation of highly oxygenated low-volatility products from cresol oxidation, *Atmos. Chem. Phys.*, 17(5), 3453–3474, doi:10.5194/acp-17-3453-2017, 2017.

Scrucca, L.: On some extensions to GA package: hybrid optimisation, parallelisation and islands evolution, *arXiv preprint arXiv:1605.01931*, 2017.

Sekimoto, K., Koss, A. R., Gilman, J. B., Selimovic, V., Coggon, M. M., Zarzana, K. J., Yuan, B., Lerner, B. M., Brown, S. S., Warneke, C., Yokelson, R. J., Roberts, J. M. and de Gouw, J.: High- and low-temperature pyrolysis profiles describe volatile organic compound emissions from western US wildfire fuels, *Atmos. Chem. Phys. Discussions*, 1–39, doi:10.5194/acp-2018-52, 2018.

Shrivastava, M. K., Lane, T. E., Donahue, N. M., Pandis, S. N. and Robinson, A. L.: Effects of gas particle partitioning and aging of primary emissions on urban and regional organic aerosol concentrations, *J. Geophys. Res.*, 113(D18), doi:10.1029/2007JD009735, 2008.

Stocker, T. F., Qin, D., Plattner, G., Tignor, M., Allen, S. K., Boschung, J., Nauels, A., Xia, Y., Bex, V. and Midgley, P.: *IPCC, 2013: summary for policymakers in climate change 2013: the physical science basis, contribution of working group I to the fifth assessment report of the intergovernmental panel on climate change*, Cambridge University Press, Cambridge, New York, USA., 2013.

Stockwell, C. E., Veres, P. R., Williams, J. and Yokelson, R. J.: Characterization of biomass burning emissions from cooking fires, peat, crop residue, and other fuels with high-resolution proton-transfer-reaction time-of-flight mass spectrometry, *Atmos. Chem. Phys.*, 15(2), 845–865, doi:10.5194/acp-15-845-2015, 2015.

Stolzenburg, D., Fischer, L., Vogel, A. L., Heinritzi, M., Schervish, M., Simon, M., Wagner, A. C., Dada, L., Ahonen, L. R., Amorim, A., Baccarini, A., Bauer, P. S., Baumgartner, B., Bergen, A., Bianchi, F., Breitenlechner, M., Brilke, S., Buenrostro Mazon, S., Chen, D., Dias, A., Draper, D. C., Duplissy, J., El Haddad, I., Finkenzeller, H., Frege, C., Fuchs, C., Garmash, O., Gordon, H., He, X., Helm, J., Hofbauer, V., Hoyle, C. R., Kim, C., Kirkby, J., Kontkanen, J., Kürten, A., Lampilahti, J., Lawler, M., Lehtipalo, K., Leiminger, M., Mai, H., Mathot, S., Mentler, B., Molteni, U., Nie, W., Nieminen, T., Nowak, J. B., Ojdanic, A., Onnela, A., Passananti, M., Petäjä, T., Quéléver, L. L. J., Rissanen, M. P., Sarnela, N., Schallhart, S., Tauber, C., Tomé, A., Wagner, R., Wang, M., Weitz, L., Wimmer, D., Xiao, M., Yan, C., Ye, P., Zha, Q., Baltensperger, U., Curtius, J., Dommen, J., Flagan, R. C., Kulmala, M., Smith, J. N., Worsnop, D. R., Hansel, A., Donahue, N. M. and Winkler, P. M.: Rapid growth of organic aerosol nanoparticles over a wide tropospheric temperature range, *Proceedings of the National Academy of Sciences*, 115(37), 9122–9127, doi:10.1073/pnas.1807604115, 2018.

Strader, R., Lurmann, F. and Pandis, S. N.: Evaluation of secondary organic aerosol formation in winter, *Atmos. Environ.*, 33(29), 4849–4863, 1999.

Taira, M. and Kanda, Y.: Continuous generation system for low-concentration gaseous nitrous acid, *Anal. Chem.*, 62(6), 630–633, doi:10.1021/ac00205a018, 1990.

Tiitta, P., Leskinen, A., Hao, L., Yli-Pirilä, P., Kortelainen, M., Grigonyte, J., Tissari, J., Lamberg, H., Hartikainen, A., Kuuspalo, K., Kortelainen, A.-M., Virtanen, A., Lehtinen, K. E. J., Komppula, M., Pieber, S., Prévôt, A. S. H., Onasch, T. B., 5 Worsnop, D. R., Czech, H., Zimmermann, R., Jokiniemi, J. and Sippula, O.: Transformation of logwood combustion emissions in a smog chamber: formation of secondary organic aerosol and changes in the primary organic aerosol upon daytime and nighttime aging, *Atmospheric Chem. Phys.*, 16(20), 13251–13269, doi:10.5194/acp-16-13251-2016, 2016.

Ward, D. E. and Hardy, C. C.: Smoke emissions from wildland fires, *Environ. Int.*, 17(2–3), 117–134, doi:10.1016/0160-4120(91)90095-8, 1991.

10 Williams, L. R., Gonzalez, L. A., Peck, J., Trimborn, D., McInnis, J., Farrar, M. R., Moore, K. D., Jayne, J. T., Robinson, W. A., Lewis, D. K., Onasch, T. B., Canagaratna, M. R., Trimborn, A., Timko, M. T., Magoon, G., Deng, R., Tang, D., de la Rosa Blanco, E., Prévôt, A. S. H., Smith, K. A. and Worsnop, D. R.: Characterization of an aerodynamic lens for transmitting particles greater than 1 micrometer in diameter into the Aerodyne aerosol mass spectrometer, *Atmos. Meas. Tech.*, 6(11), 3271–3280, doi:10.5194/amt-6-3271-2013, 2013.

15 World Energy Council (2016): World-Energy-Resources_SummaryReport_2016.pdf, [online] Available from: https://www.worldenergy.org/wp-content/uploads/2016/10/World-Energy-Resources_SummaryReport_2016.pdf (Accessed 26 September 2018), n.d.

World Health Organization: IARC: Outdoor air pollution a leading environmental cause of cancer deaths. No. 221, World Health Organization, 2013.

20 Zhang, X., Cappa, C. D., Jathar, S. H., McVay, R. C., Ensberg, J. J., Kleeman, M. J. and Seinfeld, J. H.: Influence of vapor wall loss in laboratory chambers on yields of secondary organic aerosol, *Proceedings of the National Academy of Sciences*, 111(16), 5802–5807, doi:10.1073/pnas.1404727111, 2014.

25

30

Table 1. Experimental parameters for the 14 smog chamber experiments used in this study, including smog chamber temperature, stove type, modified combustion efficiency (MCE), and the intial concentrations of POA and OGs.

Expt.	dataset	reference	date	experimental temperature (°C)	stove type	MCE	POA (µg m ⁻³)	OGs (µg m ⁻³)
1	Set1	Bertrand et al. 2017	29.10.2015	2	stove 1	0.85	126	4039
2		Bertrand et al. 2017	30.10.2015	2	stove 1	0.84	179	7862
3		Bertrand et al. 2017	04.11.2015	2	stove 1	0.83	73	3694
4		Bertrand et al. 2017	05.11.2015	2	stove 1	0.91	10	948
5		Bertrand et al. 2017	06.11.2015	2	stove2	0.80	42	1839
6		Bertrand et al. 2017	07.11.2015	2	stove2	0.87	35	2007
7		Bertrand et al. 2017	09.11.2015	2	stove2	0.82	44	3379
8	Set2	Bruns et al. 2016, Ciarelli et al. 2017	02.04.2014	-10	stove 3	0.97	9	301
9		Bruns et al. 2016, Ciarelli et al. 2017	17.03.2014	-10	stove 3	n.a.	12	1024
10		Bruns et al. 2016	25.03.2014	15	stove 3	0.97	22	526
11		Bruns et al. 2016	27.03.2014	15	stove 3	0.97	15	645
12		Bruns et al. 2016	28.03.2014	15	stove 3	0.97	17	1368
13		Bruns et al. 2016	29.03.2014	15	stove 3	0.97	18	1096
14		Bruns et al. 2016	30.03.2014	15	stove 3	0.97	18	910

5 n.a.: not available.

Table 2. Reported average reaction rate constants (10^{-11} cm 3 molec $^{-1}$ s $^{-1}$) towards OH per family at the beginning of each experiment, including average reactivity (AVG) and standard deviation (STDEV).

Expt.	Furans	SAH	PAH	OxyAH	OVOC $_{c \geq 6}$	OVOC $_{c < 6}$
1	2.96	1.90	2.90	1.94	0.66	1.16
2	2.97	1.86	2.99	2.05	0.70	1.25
3	3.04	1.88	2.95	2.07	0.66	1.19
4	2.79	2.02	2.84	2.38	0.62	1.16
5	3.04	2.10	2.73	2.57	0.60	1.12
6	3.04	1.88	2.83	2.09	0.59	1.11
7	2.92	1.93	2.80	2.05	0.67	1.21
8	3.09	2.28	3.36	3.74	0.88	1.40
9	3.65	2.37	3.76	5.58	0.69	1.48
10	3.15	2.34	3.27	4.41	0.59	1.44
11	3.11	2.34	3.07	4.04	0.60	1.57
12	3.04	2.23	2.50	2.32	0.75	1.39
13	3.02	2.33	3.48	2.98	0.72	1.41
14	2.96	2.36	3.58	4.40	0.77	1.50
AVG	3.06	2.13	3.08	3.04	0.68	1.31
STDEV	0.19	0.21	0.36	1.17	0.08	0.16

Optimization

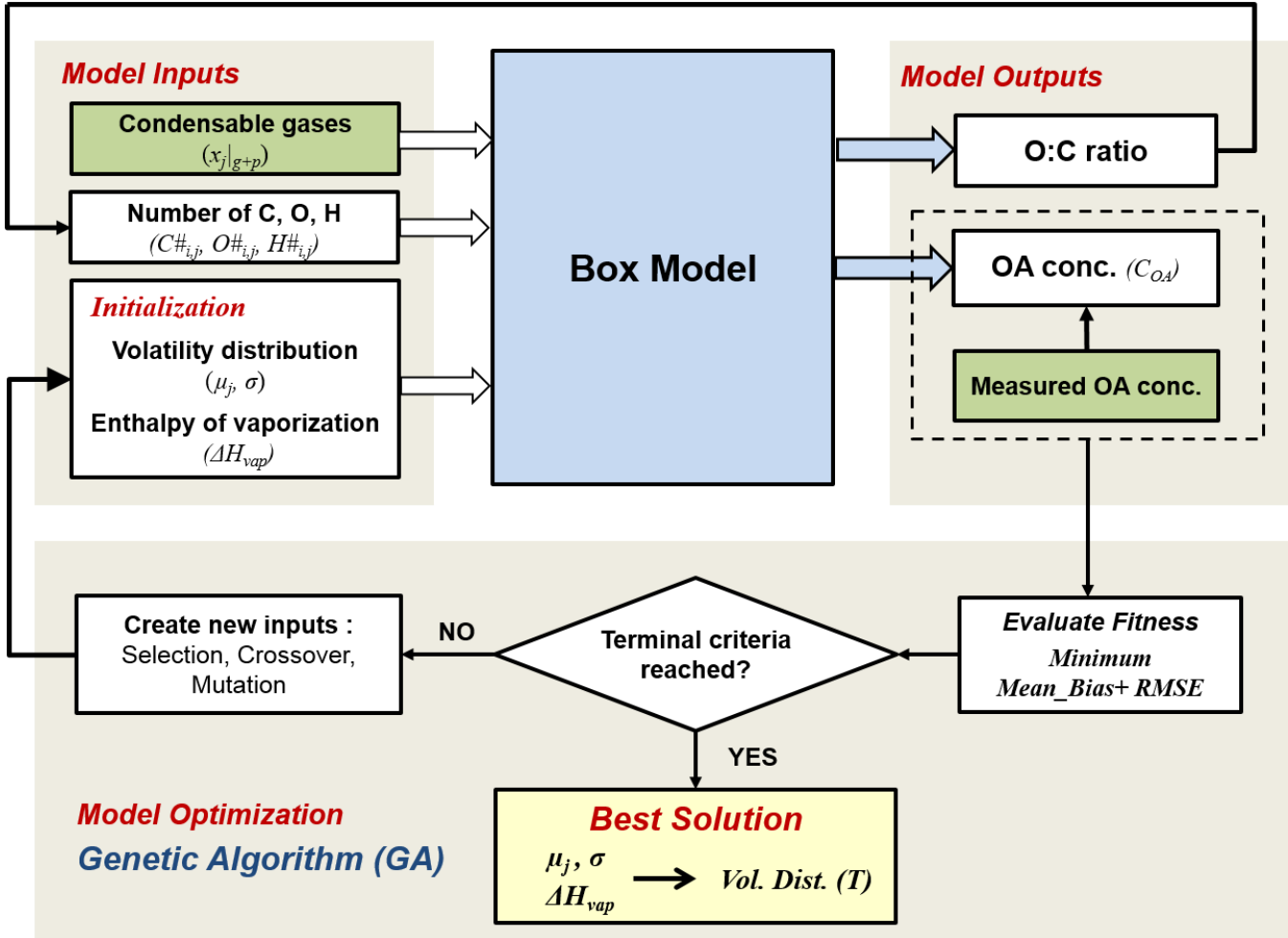


Figure 1. Schematic of the modelling framework. The box model simulates the formation of SOA from each precursor class j in volatility bins i . The best solution of the initialized input parameters volatility distribution (described as mean value of $\log C^*$ for each precursor class μ_j and standard deviation σ) and enthalpy of vaporization (ΔH_{vap}) parameters are optimized by a genetic algorithm, using minimum mean bias and root mean square error (RMSE) between modelled and measured OA concentration as the fitness function. Green boxes represent measured data from the chamber experiments.

5

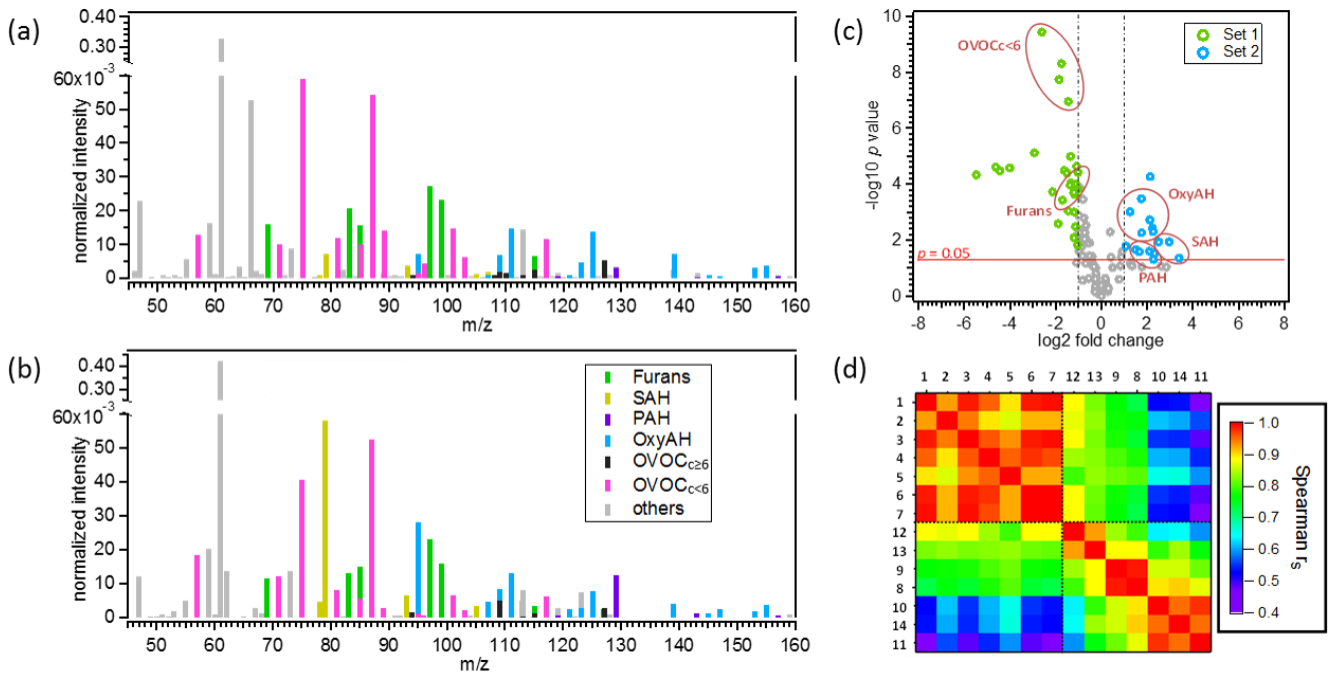


Figure 2. Comparison of the OG emissions between the two sets of experiments. Panels (a) and (b) display average primary OGs mass spectra from Set1 (representing the smoldering phase) and Set2 (representing mainly the flaming phase), respectively. Spectra are normalized to the initial total OG concentration in $\mu\text{g m}^{-3}$. Compounds are color coded by chemical classes. c) p -value versus fold change comparing the fingerprints of primary OGs between the two sets of experiments. The fold change was calculated as the ratio of the intensities of each ion normalized to the total signal, between Set2 and Set1 averaged across experiments. Data points above $p = 0.05$ have significantly different contributions to the total OGs between the two sets of experiments. Blue colored data points on the right hand side designate compounds enriched in the emissions from Set2 while green colored data points on the left hand side designate compounds enriched in the emissions from Set1. d) Spearman correlation matrix for the primary OGs mass spectra between all experiments highlighting the variability in the composition of the primary emissions. Each experiment is identified by an index (see Table 1) and the experiments from Set2 were reordered according to similarity with Set1.

15

20

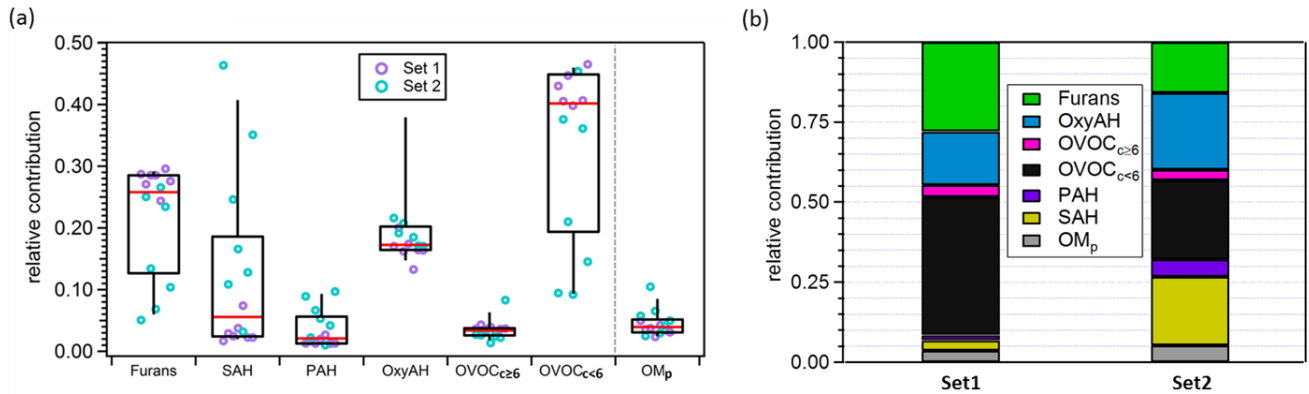


Figure 3. a) Box plot for the relative contributions to the total primary emissions of the different precursor classes and of OM_p averaged between experiments. OM_p is the total semi-volatile and low-volatility organic matter calculated by means of the VBS model assuming the volatility distribution from May et al. (2013) and using as input the measured organic aerosol (OA) mass. The top and bottom whiskers represent the 90th and 10th percentiles, respectively, while the top, middle and bottom lines of the boxes show the 75th, 50th and 25th percentiles, respectively. The circles represent each single experiment from the two datasets investigated.

b) Average contributions of different precursor families and OM_p for Set1 and Set2.

10

15

20

25

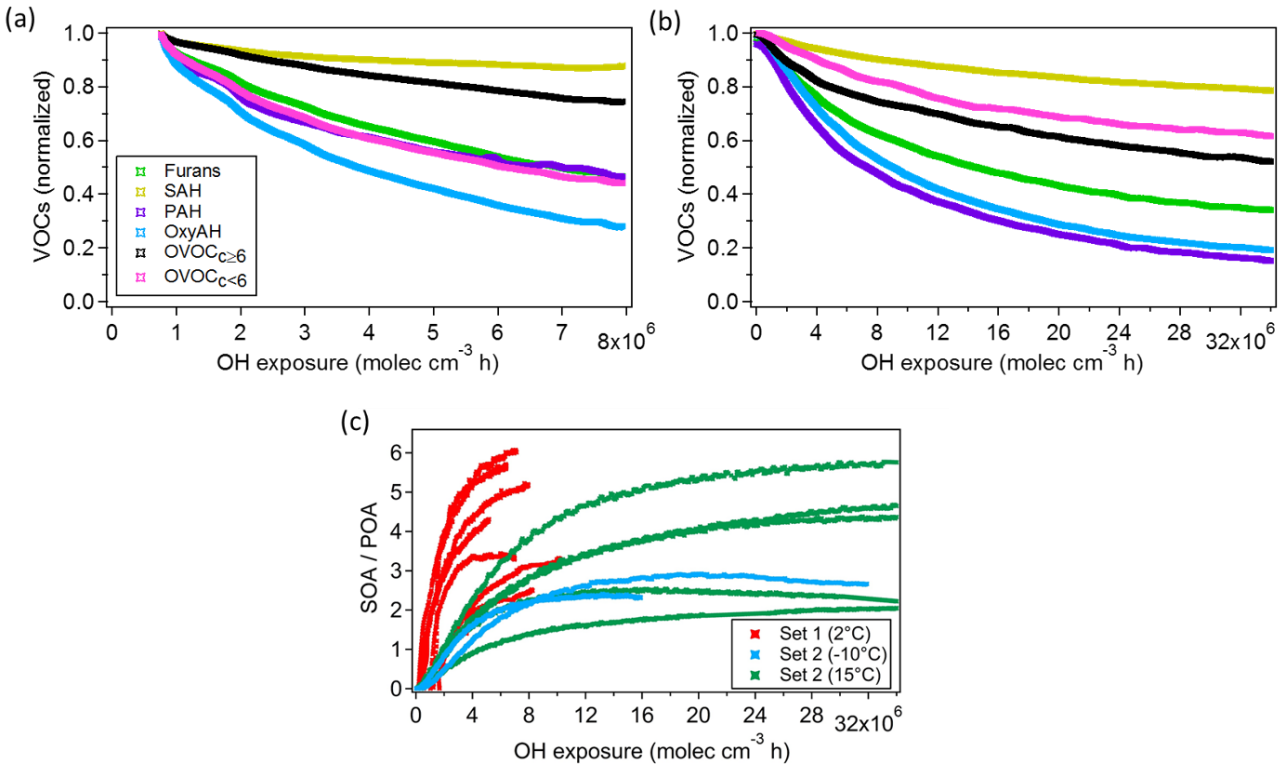


Figure 4. Average consumption of SOA precursor classes against average OH exposure for Set1 (a) and Set2 (b). The observed decay of SOA precursor families (OGs) as described in Eq. (1) is due to both oxidation processes and dilution in the chamber. 5 (c) SOA to POA ratio for each experiment against average OH exposure colored according to experimental temperatures (2°C , -10°C , 15°C).

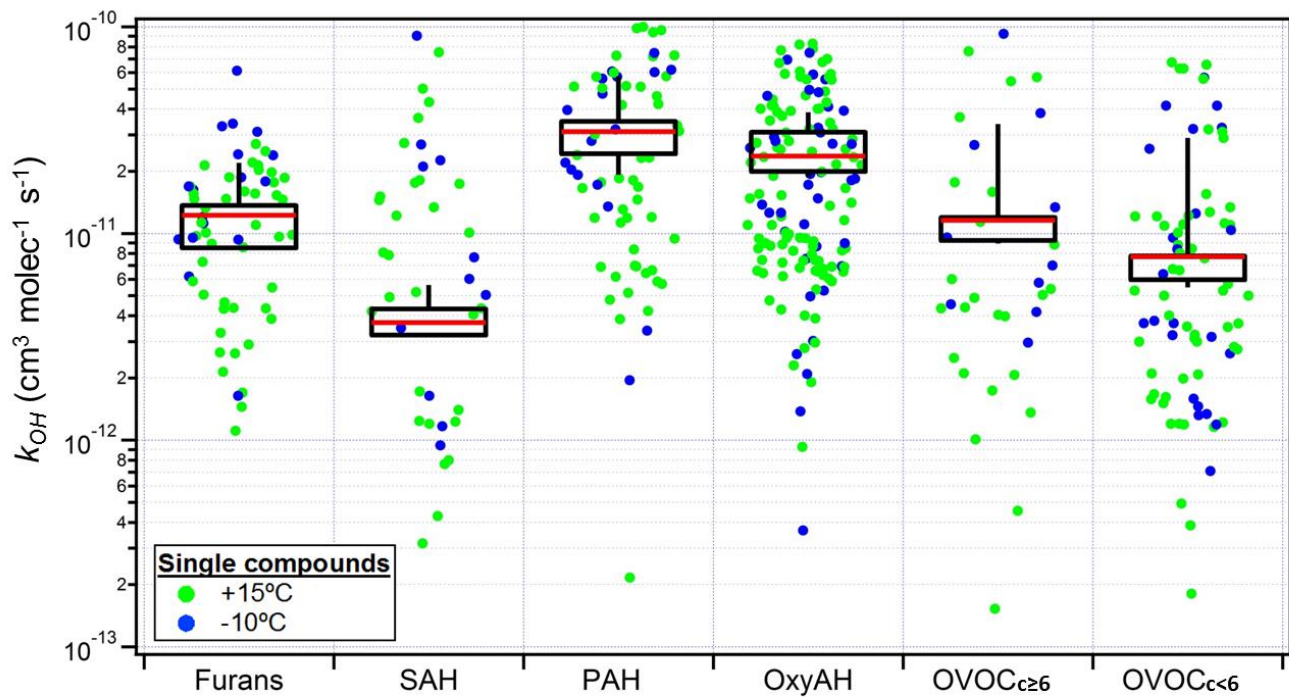


Figure 5. Box plot of mass weighted average OH reaction rate constants (k_{OH}) determined for each precursor class from Bruns et al. (2016) for Set2 only (see Table S3). The individual k_{OH} values for all compounds are also shown for all experiments, color coded according to the experimental temperatures. The top and bottom whiskers represent the 90th and 10th percentiles, while the top, 5 middle and bottom lines of the boxes show the 75th, 50th, and 25th percentiles.

10

15

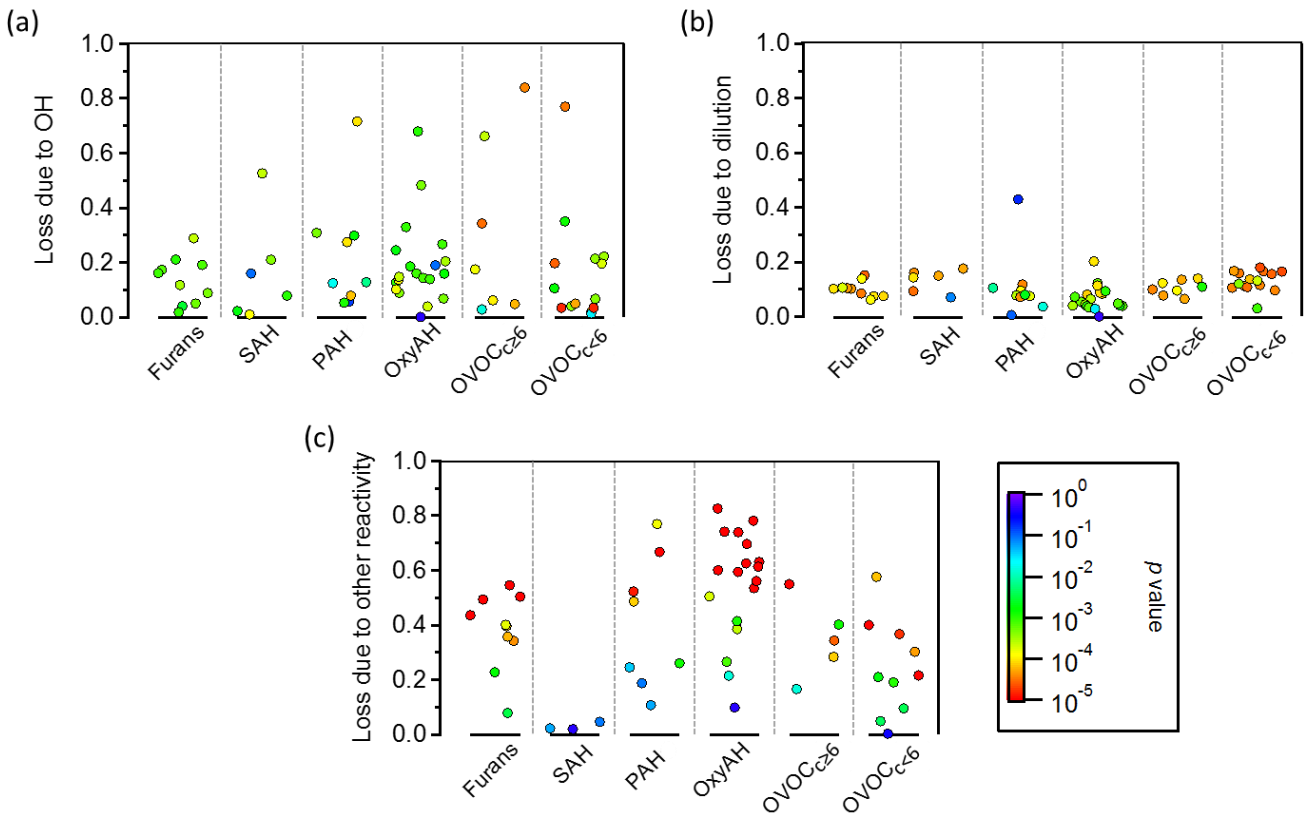


Figure 6. Fraction of consumed precursor compounds for Set1 by OH oxidation (a), dilution (b) and other reactivity (c) at the end of the experiments. Each point corresponds to a single compound averaged among experiments and normalized to the initial concentration. The color legend represents the statistically significant deviation from zero reactivity with the investigated reactant

5 (p value).

10

15

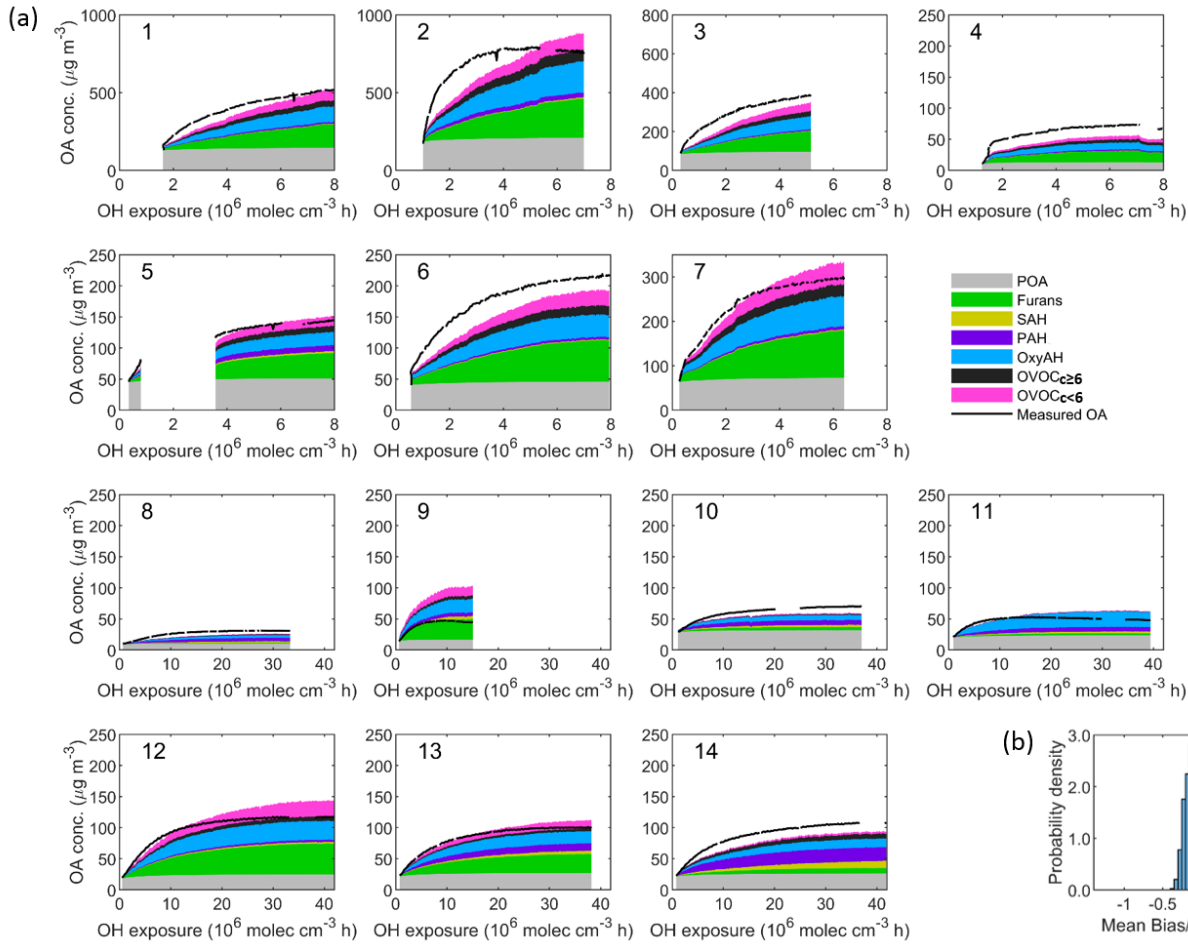


Figure 7. a) Comparison between the sum of simulated organic aerosol (OA) concentrations from different precursor families and the measured OA concentration as a function of the OH exposure for each smog chamber experiment. Set1 (Expt. 1-7, 2°C) and Set2 (Expt. 8-9, -10°C and Expt. 10-14, 15°C). **b)** Probability distribution of mean bias weighted by the average measured OA concentration. The resulting mean bias is $-7.2 \mu\text{g m}^{-3}$ (~15%) and the root-mean-square error (RMSE) is $37.4 \mu\text{g m}^{-3}$. The model tends to underestimate the measured OA for Set1 with a mean bias of 7% while it tends to overestimate the measured OA for Set2 with a mean bias of 8%.

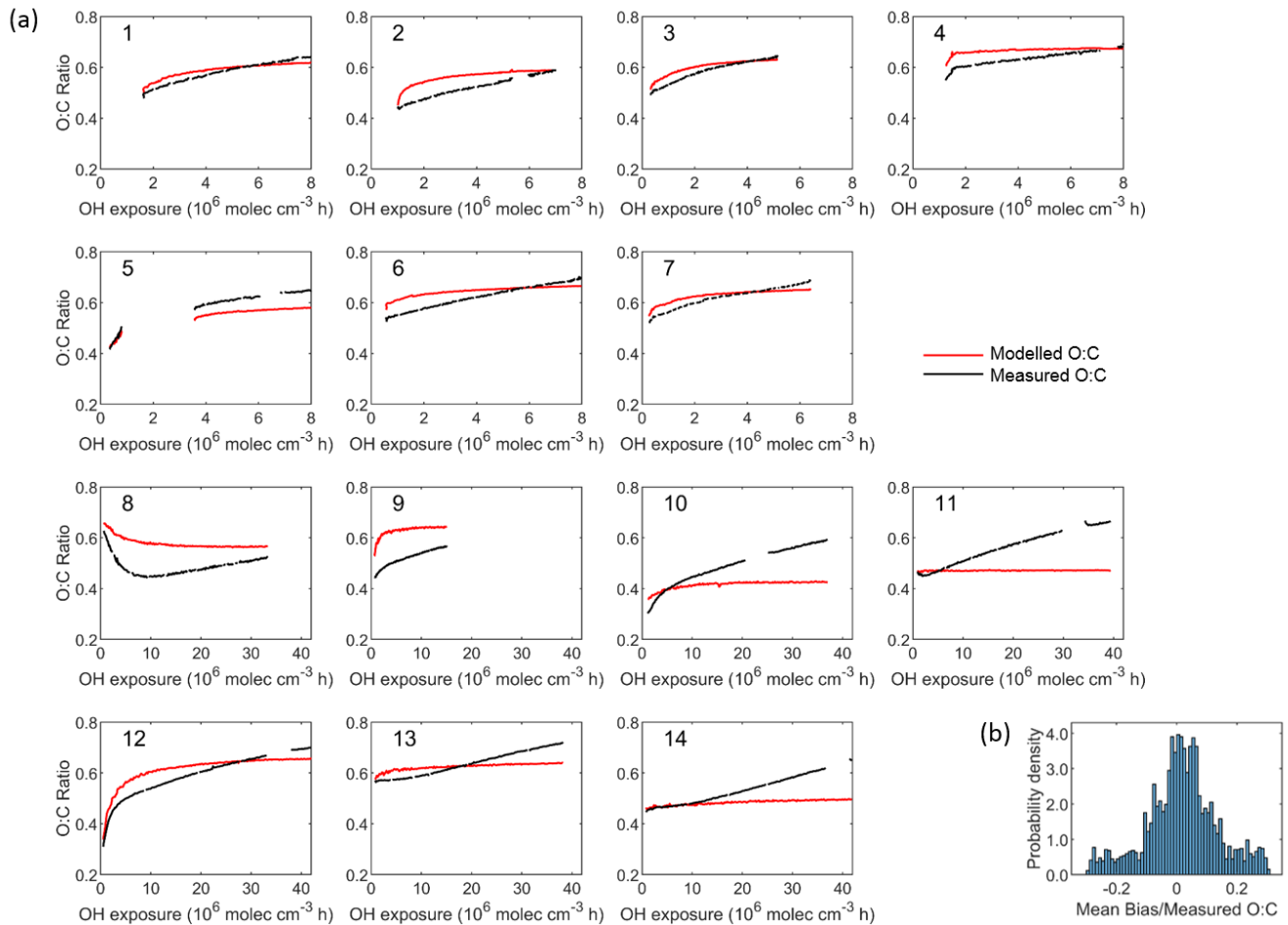
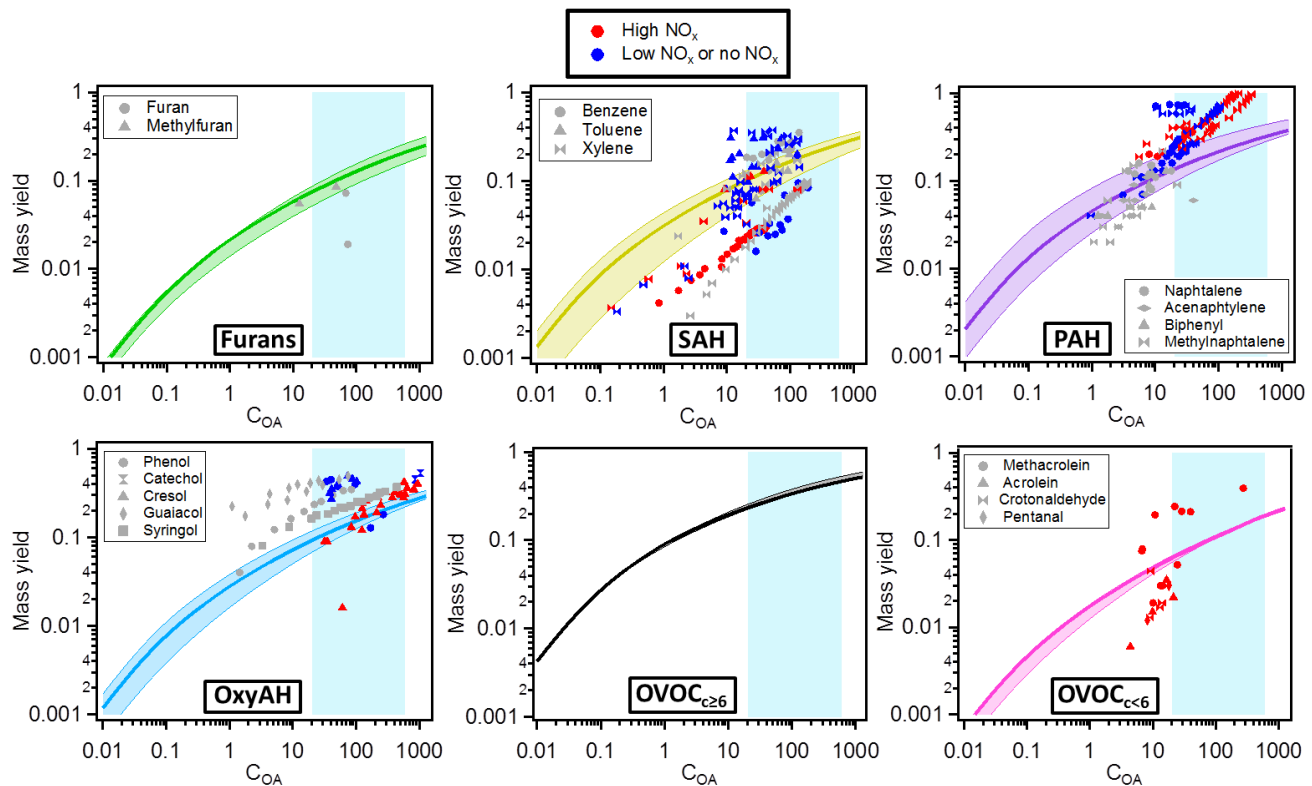


Figure 8. a) Comparison between modelled and measured O:C ratio as a function of the OH exposure for each experiment. Set1 (Expt. 1-7, 2°C) and Set2 (Expt. 8-9, -10°C and Expt. 10-14, 15°C). b) Probability distribution of the relative bias (normalized by the averaged measured O:C ratios). The resulting mean relative bias is 0.006 and the root-mean-square error (RMSE) is 0.06.



5 **Figure 9. Mass yields for each class of compounds. The solid lines represent the median values while the lower and upper limits are the 25th and 75th percentiles, respectively. The different markers in each plot are yields published in the literature for different single compounds (see Table S2). The color code denotes different NO_x regimes (red denoting high NO_x, blue low or no NO_x and grey not specified NO_x regimes). The shaded background represents the range of our experiments (20-600 $\mu\text{g m}^{-3}$), outside this shaded area yields are extrapolated from the model.**

10

15

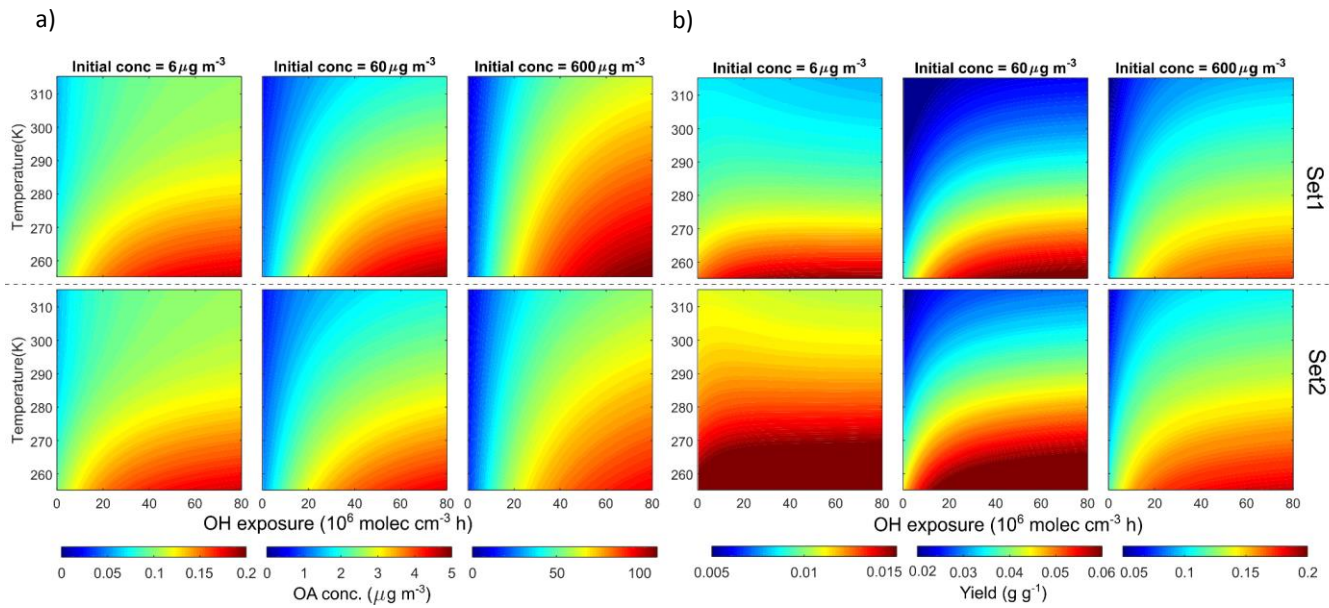


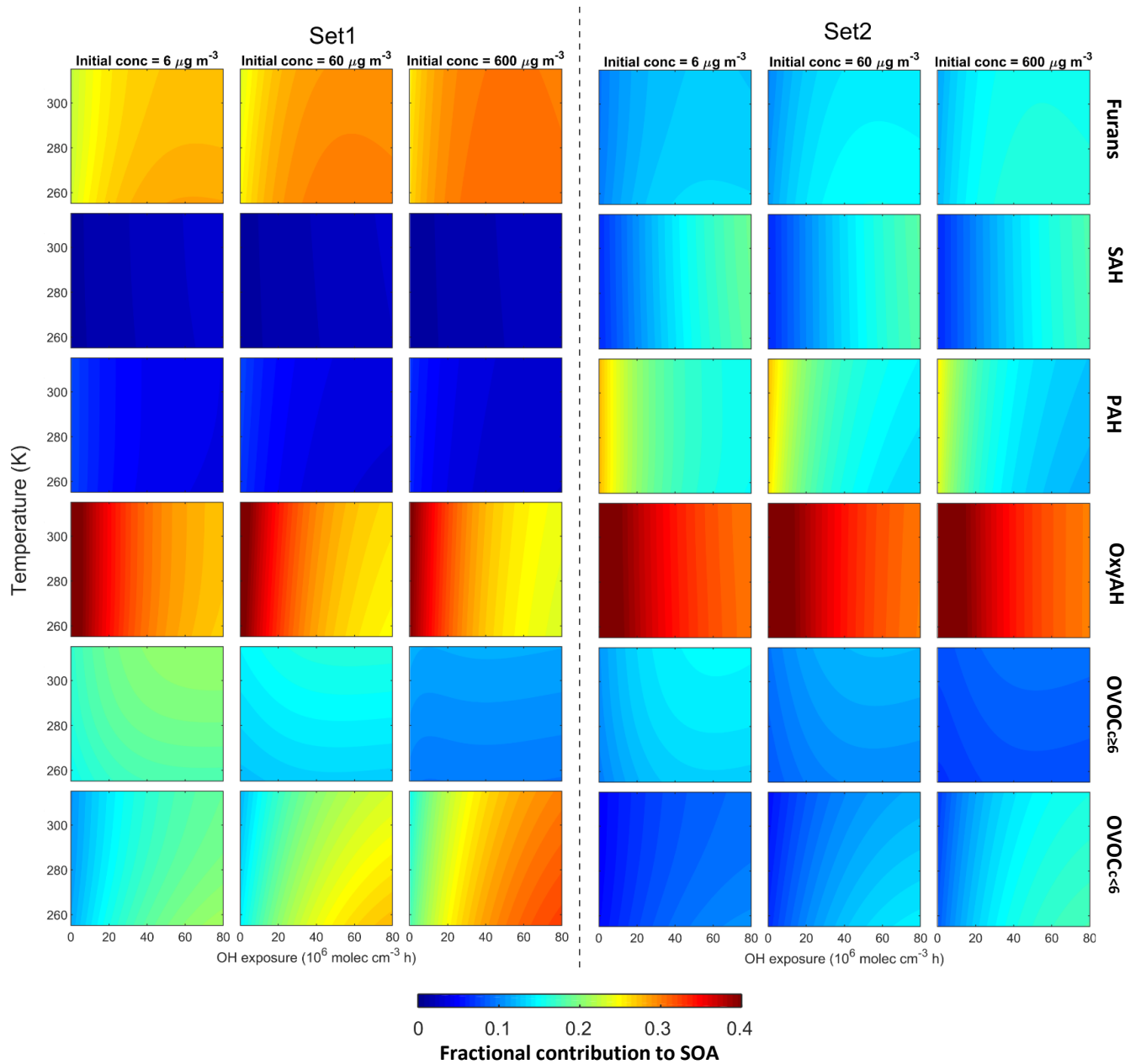
Figure 10. Modelled OA concentrations (a) and yields (b) under different temperature, OH exposure and initial OA concentrations (6, 60 and 600 $\mu\text{g m}^{-3}$). Upper and lower panels are based on Set1 and Set2, respectively. Temperature is provided in Kelvin (K) to

5 **avoid confusion with the experimental data in Celsius ($^{\circ}\text{C}$).**

10

15

20



5 **Figure 11.** Fractional contributions of the six precursor classes to SOA formation under different temperature, OH exposure, and initial OA concentrations. Left and right panels are based on Set1 and Set2, respectively. Temperature is provided in Kelvin (K) to avoid confusion with the experimental data in Celsius (°C).